MULTISCALE MODEL. SIMUL.
Vol. 10, No. 4, pp. 1369–1408

STAGGERED SCHEMES FOR FLUCTUATING HYDRODYNAMICS*

FLORENCIO BALBOA USABIAGA†, JOHN B. BELL‡, RAFAEL DELGADO-BUSCALIONI†, ALEKSANDAR DONEV§, THOMAS G. FAI§, BOYCE E. GRIFFITH¶, AND CHARLES S. PESKIN§

Abstract. We develop numerical schemes for solving the isothermal compressible and incompressible equations of fluctuating hydrodynamics on a grid with staggered momenta. We develop a second-order accurate spatial discretization of the diffusive, advective, and stochastic fluxes that satisfies a discrete fluctuation-dissipation balance and construct temporal discretizations that are at least second-order accurate in time deterministically and in a weak sense. Specifically, the methods reproduce the correct equilibrium covariances of the fluctuating fields to the third (compressible) and second (incompressible) orders in the time step, as we verify numerically. We apply our techniques to model recent experimental measurements of giant fluctuations in diffusively mixing fluids in a microgravity environment [A. Vailati et al., *Nat. Comm.*, 2 (2011), 290]. Numerical results for the static spectrum of nonequilibrium concentration fluctuations are in excellent agreement between the compressible and incompressible simulations and in good agreement with experimental results for all measured wavenumbers.

Key words. fluctuating hydrodynamics, staggered grid, giant fluctuations, fluctuation-dissipation balance

AMS subject classifications. 65M08, 65M22, 60H35, 82C31, 35R60

DOI. 10.1137/120864520

1. Introduction.

At a molecular scale, fluids are not deterministic; the state of the fluid is constantly changing and stochastic, even at thermodynamic equilibrium. Stochastic effects are important for flows in new microfluidic, nanofluidic, and microelectromechanical devices [1]; novel materials such as nanofluids [2]; biological systems such as lipid membranes [3]; Brownian molecular motors [4]; nanopores [5]; as well as processes where the effect of fluctuations is amplified by strong nonequilibrium effects, such as combustion of lean flames, capillary dynamics [6, 7], hydrodynamic instabilities [8, 9, 10], and others. Because they span the whole range of scales from the microscopic to the macroscopic [11, 12], fluctuations need to be consistently included

*Received by the editors February 2, 2012; accepted for publication (in revised form) August 8, 2012; published electronically November 29, 2012.
http://www.siam.org/journals/mms/10-4/86452.html

†Departamento de Física Teórica de la Materia Condensada, Univeridad Autónoma de Madrid, Madrid 28049, Spain (florencio.balboa@uam.es, rafael.delgado@uam.es). These authors' research was supported by the Spanish government FIS2010-22047-C0S and the Comunidad de Madrid MODELICO-CM (S2009/ESP-1691).

‡Center for Computational Science and Engineering, Lawrence Berkeley National Laboratory, Berkeley, CA 94720 (JBBell@lbl.gov). This author's research was supported by the DOE Applied Mathematics Program of the DOE Office of Advanced Scientific Computing Research under the U.S. Department of Energy under contract DE-AC02-05CH11231.

§Courant Institute of Mathematical Sciences, New York University, New York, NY 10012 (donev@courant.nyu.edu, tfai@cims.nyu.edu, peskin@courant.nyu.edu). The fourth author's research was supported by the DOE Applied Mathematics Program of the DOE Office of Advanced Scientific Computing Research under the U.S. Department of Energy under contract DE-AC02-05CH11231 and by the National Science Foundation under grant DMS-1115341. The fifth author's research was supported by the DOE Computational Science Graduate Fellowship under grant DE-FG02-97ER25308.

¶Department of Medicine, Leon H. Charney Division of Cardiology, New York University School of Medicine, New York, NY 10016 (griffith@cims.nyu.edu). This author's research was supported by the National Science Foundation under awards OCI 1047734 and DMS 1016554.

in all levels of description [13]. Thermal fluctuations are included in the fluctuating Navier–Stokes (NS) equations and related continuum Langevin models [14, 15] through stochastic forcing terms, as first proposed by Landau and Lifshitz [16]. Numerically solving the continuum equations of *fluctuating hydrodynamics* [17] is difficult because of the presence of nontrivial dynamics at all scales and the existence of a nontrivial invariant measure (equilibrium distribution).

Several numerical approaches for fluctuating hydrodynamics have been proposed. The earliest work by Garcia et al. [18] developed a simple scheme for the stochastic heat equation and the linearized one-dimensional fluctuating NS equations. Ladd and others have included stress fluctuations in (isothermal) lattice Boltzmann methods for some time [19]. Moseler and Landman [8] included the stochastic stress tensor of Landau and Lifshitz in the lubrication equations and obtained good agreement with their molecular dynamics simulation in modeling the breakup of nanojets. Sharma and Patankar [20] developed a fluid-structure coupling between a fluctuating incompressible solver and suspended Brownian particles. Coveney, De Fabritiis, Delgado-Buscalioni, and co-workers have also used the fluctuating isothermal NS equations in a hybrid scheme, coupling a continuum fluctuating solver to a molecular dynamics simulation of a liquid [21, 22, 23]. Atzberger, Kramer, and Peskin have developed a version of the immersed boundary method that includes fluctuations [24, 25]. Voulgarakis and Chu [26] developed a staggered scheme for the isothermal compressible equations as part of a multiscale method for biological applications, and a similar staggered scheme was also described in [27].

Some of us have recently developed techniques for analyzing the weak accuracy of finite-volume methods for solving the types of stochastic PDEs that appear in fluctuating hydrodynamics [28]. The analysis emphasizes the necessity to maintain fluctuation-dissipation balance in spatio-temporal discretizations [28], thus reproducing the Gibbs–Boltzmann distribution dictated by equilibrium statistical mechanics. Based on previous work by Bell, Garcia, and Williams [29, 30], a *collocated* spatial discretization for the compressible equations of fluctuating hydrodynamics has been developed and combined with a stochastic third-order Runge–Kutta (RK3) temporal integrator [28]. The collocated spatial discretization has been used to construct a strictly conservative particle-continuum hybrid method [13] and to study the contribution of advection by thermal velocities to diffusive transport [31].

A *staggered* spatial discretization is advantageous for incompressible flows because it leads to a robust idempotent discrete projection operator [32, 33]. Staggered schemes have previously been developed for isothermal compressible [26] and incompressible flow [20], without, however, carefully assessing discrete fluctuation-dissipation balance. Here we present and test an explicit compressible and a semi-implicit incompressible scheme for fluctuating hydrodynamics on uniform staggered grids. Both methods use closely related spatial discretizations but very different temporal discretizations. In the spatial discretization, we ensure an accurate spectrum of the steady-state fluctuations by combining a locally conservative finite-volume formulation, a nondissipative (skew-symmetric) advection discretization, and discretely dual divergence and gradient operators. For compressible flow, we employ an explicit RK3 scheme [28] since the time step is limited by the speed of sound and the dissipative terms can be treated explicitly. For incompressible flow, we use a semi-implicit unsplit method first proposed in [34], which allows us to take large time steps that underresolve the fast momentum diffusion at grid scales but still obtain the correct steady-state covariances of fluctuations.

Thermal fluctuations in nonequilibrium systems in which a constant (tempera-

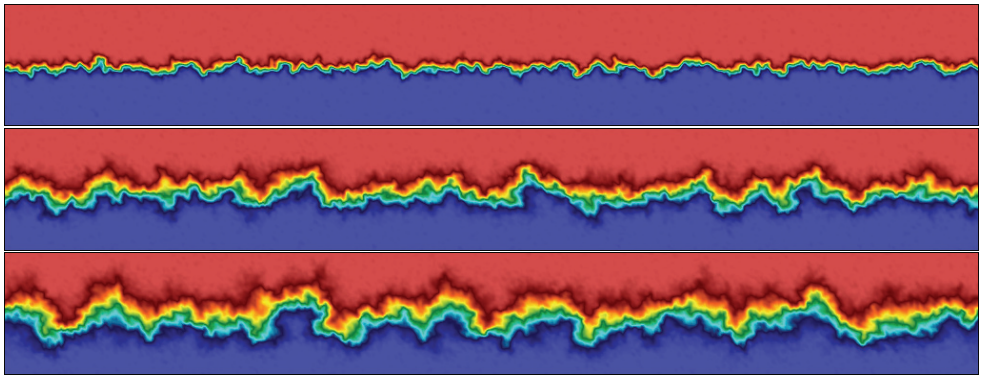

FIG. 1. *Snapshots of concentration showing the development of a* rough *diffusive interface between two miscible fluids in zero gravity. We show three points in time (top to bottom), starting from an initially perfectly flat interface (phase separated system). These figures were obtained using the incompressible code described in section* 4.1.

ture, concentration, velocity) gradient is imposed externally exhibit remarkable behavior compared to equilibrium systems. Most notably, external gradients can lead to *enhancement* of thermal fluctuations and to *long-range* correlations between fluctuations [17, 35, 36, 37, 38]. This phenomenon can be illustrated by considering concentration fluctuations in an isothermal mixture of two miscible fluids in the presence of a strong concentration gradient $\boldsymbol{\nabla} c$, as in the early stages of diffusive mixing between initially separated fluid components. As illustrated in Figure 1, the interface between the fluids, instead of remaining flat, develops large-scale roughness that reaches a pronounced maximum until gravity or boundary effects intervene. These *giant fluctuations* [39, 40, 41] during free diffusive mixing have been observed using light scattering and shadowgraphy techniques [12, 42, 43, 44, 45], finding good but imperfect agreement between the predictions of a simplified fluctuating hydrodynamic theory and experiments. Recent experiments have taken advantage of the enhancement of the nonequilibrium fluctuations in a microgravity environment aboard the FOTON M3 spaceship [12, 44] and have demonstrated the appearance of fractal diffusive fronts like those illustrated in Figure 1. In the absence of gravity, the density mismatch between the two fluids does not change the qualitative nature of the nonequilibrium fluctuations, and in this work we focus on mixtures of dynamically identical fluids.

Before discussing spatio-temporal discretizations, we review the continuum formulation of the equations of fluctuating hydrodynamics and their crucial properties in section 2. In particular, we discuss the steady-state covariances of the fluctuating fields for systems in thermal equilibrium as well as fluid mixtures with an imposed concentration gradient. In section 3.1 we focus on the temporal discretization in the spirit of the method of lines. For the compressible equations, we employ a previously developed explicit three-stage Runge–Kutta scheme that is third-order weakly accurate [28]. For the incompressible equations, we employ a second-order accurate predictor-corrector approach, each stage of which is a semi-implicit (Crank–Nicolson) discretization of the unsteady Stokes equations, solved effectively using a projection method as a preconditioner [34]. In section 3.2.5 we describe a conservative staggered spatial discretization of the diffusive, stochastic, and advective fluxes. We maintain discrete fluctuation-dissipation balance [28, 46] by ensuring duality between the dis-

crete divergence and gradient operators and by using a skew-adjoint discretization of advection. We verify the weak order of accuracy for both the compressible and incompressible algorithms in section 4. In section 5 we model the nonequilibrium concentration fluctuations in a fluid mixture under an applied temperature gradient and compare the numerical results to recent experimental measurements [12, 44].

1.1. Deterministic hydrodynamic equations. Motivated by the microgavity experiments studying giant fluctuations [12, 44], we consider an ideal solution of a macromolecule with molecular mass M in a solvent. At the macroscopic level, the hydrodynamics of such a mixture can be modeled with an extended set of NS equations for the mass density $\rho = \rho_1 + \rho_2$, where ρ_1 is the mass density of the solute, $\boldsymbol{v}$ is the center-of-mass velocity, $c = \rho_1/\rho$ is the mass concentration, and T is the temperature [17, 30]. In many situations of interest the temperature $T(\boldsymbol{r}, t) \equiv T(\boldsymbol{r})$ can be taken as fixed [17, 39, 45] since temperature fluctuations do not couple to other variables. The fixed-temperature *compressible* NS equations for an ideal mixture of two miscible fluids are

$$D_t \rho = -\rho (\boldsymbol{\nabla} \cdot \boldsymbol{v}), \tag{1}$$

$$\rho (D_t \boldsymbol{v}) = -\boldsymbol{\nabla} P + \boldsymbol{\nabla} \cdot \left[\eta \overline{\boldsymbol{\nabla}} \boldsymbol{v} + \zeta (\boldsymbol{\nabla} \cdot \boldsymbol{v}) \boldsymbol{I} \right] + \boldsymbol{f}_v, \tag{2}$$

$$\rho (D_t c) = \boldsymbol{\nabla} \cdot [\rho \chi (\boldsymbol{\nabla} c + c (1 - c) S_T \boldsymbol{\nabla} T)] + f_c, \tag{3}$$

supplemented with appropriate boundary conditions. Here $D_t \square = \partial_t \square + \boldsymbol{v} \cdot \boldsymbol{\nabla} (\square)$ is the advective derivative, $\overline{\boldsymbol{\nabla}} \boldsymbol{v} = (\boldsymbol{\nabla} \boldsymbol{v} + \boldsymbol{\nabla} \boldsymbol{v}^T) - 2 (\boldsymbol{\nabla} \cdot \boldsymbol{v}) \boldsymbol{I}/3$ is the symmetrized strain rate, $P(\rho, c; T)$ is the pressure as given by the equation of state, and $\boldsymbol{f}_v$ and f_c are external forcing (source) terms. The shear viscosity η, bulk viscosity ζ, mass diffusion coefficient χ, and Soret coefficient S_T can, in general, depend on the state. We make several physically motivated approximations, including neglecting barodiffusion, as we describe and justify next.

We will assume that the two species in the mixture are almost identical, meaning that none of the fluid properties is affected by concentration. In this sense the macromolecules are assumed to be simple (passive) tracer particles. This is a reasonable approximation for small concentrations $c \ll 1$ since the presence of small amounts of macromolecules causes small changes in the properties of the solution. In the giant fluctuation experiments in microgravity conditions the concentration is at most a few percent [12, 44], justifying the assumption that the equation of state is independent of concentration, $P(\rho, c; T) = P(\rho; T)$. This approximation also allows us to neglect barodiffusion since the barodiffusion coefficient is a thermodynamic rather than a transport coefficient and vanishes for such an equation of state.

Because the temperature varies by only a few percent across the sample in the giant fluctuation experiments modeled in section 5, we take the system to be *isothermal*, and thus the temperature $T = T_0$ is constant. However, we retain the crucial Soret term by taking $S_T \boldsymbol{\nabla} T$ to be a specified constant. Note that the Soret term is a transport coefficient unlike the barodiffusion coefficient and can be positive or negative.

For liquids, the equation of state is usually very stiff, which means that the (isothermal) sound speed $c_T^2 = \partial P/\partial \rho$ is very large. Density is therefore nearly constant, and an incompressible approximation will be appropriate as a means to avoid the stiffness. An alternative, employed, for example, in the lattice Boltzmann method, is to keep the simpler compressible equations (and thus avoid elliptic constraints) but to make the speed of sound much smaller than the actual speed of sound but still large

enough that density variations are negligible. This is the sense in which we will use the compressible equations (1)–(3), although we emphasize that there are situations in which it is actually important to solve these equations with the proper equation of state [26, 47].

Under the assumption that density variations are small, it is not important what precise dependence of the transport coefficients and equation of state on the density is used. We will therefore assume that $P = P(\rho) = P_0 + (\rho - \rho_0)\, c_T^2$, where c_T is a spatially constant isothermal speed of sound. The value of c_T can be a parameter that lets us tune the compressibility or the physical speed of sound. Furthermore, we will assume that the viscosity and Soret coefficient are constants independent of the density and that the product $\rho\chi = \rho_0\chi_0$ is constant. Recalling that in the experiments $c \ll 1$ so that $c\,(1-c) \approx c$, all of these approximations allow us to write the viscous term in the momentum equation in the "Laplacian" form

$$\boldsymbol{\nabla} \cdot \left[\eta \overline{\boldsymbol{\nabla}} \boldsymbol{v} + \zeta\, (\boldsymbol{\nabla} \cdot \boldsymbol{v})\, \boldsymbol{I}\right] \rightarrow \eta \boldsymbol{\nabla}^2 \boldsymbol{v} + \left(\zeta + \frac{\eta}{3}\right) \boldsymbol{\nabla}\, (\boldsymbol{\nabla} \cdot \boldsymbol{v})\,. \tag{4}$$

Similarly, the diffusive term in the concentration equation can be written as

$$\boldsymbol{\nabla} \cdot \left[\rho\chi\, (\boldsymbol{\nabla} c + c\,(1-c)\, S_T \boldsymbol{\nabla} T)\right] \rightarrow \rho\left[\chi \boldsymbol{\nabla}^2 c + \boldsymbol{\nabla} \cdot (c \boldsymbol{v}_s)\right], \tag{5}$$

where the spatially constant velocity difference between the two species is denoted with $\boldsymbol{v}_s = \chi S_T \boldsymbol{\nabla} T$.

With all of these simplifications, the equations we actually solve numerically are

$$D_t \rho = -\,\rho\, (\boldsymbol{\nabla} \cdot \boldsymbol{v})\,, \tag{6}$$

$$\rho\, (D_t \boldsymbol{v}) = -\, c_T^2 \boldsymbol{\nabla} \rho + \eta \boldsymbol{\nabla}^2 \boldsymbol{v} + \left(\zeta + \frac{\eta}{3}\right) \boldsymbol{\nabla}\, (\boldsymbol{\nabla} \cdot \boldsymbol{v}) + \boldsymbol{f}_v, \tag{7}$$

$$\rho\, (D_t c) = \rho\left[\chi \boldsymbol{\nabla}^2 c + \boldsymbol{\nabla} \cdot (c \boldsymbol{v}_s)\right] + f_c, \tag{8}$$

where all model parameters are constants.

We note that none of the simplifying approximations we make above is necessary in principle. At the same time, not making such approximations requires knowing a number of physical properties of the fluids, for example, the concentration dependence of the Soret coefficient S_T. Such information is difficult to obtain experimentally, and in any case, the known dependence is very weak and we believe it will not affect the results we present to within measurement or statistical error bars. Furthermore, accounting for the concentration dependence of the equation of state in the incompressible limit requires using variable-density low Mach number equations [48, 49] instead of the incompressible equations since, in general, $\boldsymbol{\nabla} \cdot \boldsymbol{v} \neq 0$ [50]. Extension of our algorithms to these variable-density variable-coefficient low Mach equations is possible but nontrivial and will be considered in future work.

2. Fluctuating hydrodynamics. At mesoscopic scales the hydrodynamic behavior of fluids can be described with continuum stochastic PDEs of Langevin type [14, 15], as proposed by Landau and Lifshitz [16] and later justified by formal coarse-graining procedures [51]. Such equations can formally be justified as a central limit theorem for the Gaussian behavior of the thermal fluctuations around the mean, at least in certain simpler systems [52, 53]. What emerges is that the (mesoscopic) thermal fluctuations can be described by the very same hydrodynamic equations describing the macroscopic behavior, *linearized* around the mean solution, and with added stochastic forcing terms that ensure a fluctuation-dissipation balance principle [54].

Solving these linearized equations numerically requires first solving the deterministic equations for the mean and then solving the fluctuating equations linearized around the mean. The linearization typically contains many more terms than the nonlinear deterministic terms due to the chain rule. Such a two-step process is much more cumbersome than solving the nonlinear equations. Furthermore, a linearization has no hope of capturing any possible nonlinear feedback of the fluctuations on the mean flow, which is known to have physical significance [31].

Therefore, we follow an alternative approach in which the stochastic forcing terms are directly added to the nonlinear equations (6)–(8), but with an amplitude proportional to a parameter ϵ that controls how far from linearity the equations are. In fluctuating hydrodynamics, to ensure mass and momentum conservation, the stochastic terms are the divergence of a stochastic flux,

$$\boldsymbol{f}_v = \epsilon^{\frac{1}{2}} \boldsymbol{\nabla} \cdot \boldsymbol{\Sigma} \quad \text{and} \quad f_c = \epsilon^{\frac{1}{2}} \boldsymbol{\nabla} \cdot \boldsymbol{\Psi}, \tag{9}$$

where the capital Greek letters denote stochastic fluxes that are modeled as white-noise Gaussian random fields. A detailed discussion of why there are no diffusive and stochastic fluxes in the density equation is given in [55]. For the linearized equations, we can fix $\epsilon = 1$, and the covariances of $\boldsymbol{\Sigma}$ and $\boldsymbol{\Psi}$ can be derived from the fluctuation-dissipation balance principle, as explained well in the book [17]. The covariance of the stochastic stress tensor $\boldsymbol{\Sigma}$ is not a positive definite matrix, so there are many choices for how to express the stochastic stress, especially if additional bulk viscosity is included [56]. We have based our implementation on a formulation that requires the fewest possible random numbers [51, 57],

$$\boldsymbol{\Sigma} = \boldsymbol{\Sigma}_s + \boldsymbol{\Sigma}_p = \sqrt{2\eta k_B T}\, \widetilde{\boldsymbol{\mathcal{W}}}_{\boldsymbol{v}} + \left(\sqrt{\frac{\zeta k_B T}{3}} - \frac{\sqrt{2\eta k_B T}}{3} \right) \operatorname{Tr}\left(\widetilde{\boldsymbol{\mathcal{W}}}_{\boldsymbol{v}} \right) \boldsymbol{I}, \tag{10}$$

$$\boldsymbol{\Psi} = \sqrt{2\chi \rho M\, c(1-c)}\, \boldsymbol{\mathcal{W}}_c, \tag{11}$$

where $\widetilde{\boldsymbol{\mathcal{W}}}_{\boldsymbol{v}} = (\boldsymbol{\mathcal{W}}_{\boldsymbol{v}} + \boldsymbol{\mathcal{W}}_{\boldsymbol{v}}^T)/\sqrt{2}$ is a symmetric Gaussian random tensor field, and the $\sqrt{2}$ in the denominator accounts for the reduction in variance due to the averaging. Here $\boldsymbol{\mathcal{W}}_{\boldsymbol{v}}$ and $\boldsymbol{\mathcal{W}}_c$ are mutually uncorrelated white-noise random Gaussian tensor and vector fields with uncorrelated components

$$\left\langle \mathcal{W}_{ij}^{(\boldsymbol{v})}(\boldsymbol{r},t) \mathcal{W}_{kl}^{(\boldsymbol{v})}(\boldsymbol{r}',t') \right\rangle = (\delta_{ik}\delta_{jl})\, \delta(t-t')\delta(\boldsymbol{r}-\boldsymbol{r}'), \tag{12}$$

$$\left\langle \mathcal{W}_{i}^{(c)}(\boldsymbol{r},t) \mathcal{W}_{j}^{(c)}(\boldsymbol{r}',t') \right\rangle = (\delta_{ij})\, \delta(t-t')\delta(\boldsymbol{r}-\boldsymbol{r}'). \tag{13}$$

Similar covariance expressions apply in the Fourier domain as well if position $\boldsymbol{r}$ (time t) is replaced by wavevector $\boldsymbol{k}$ (wavefrequency ω) and $\langle \mathcal{W}_\alpha \mathcal{W}_\beta \rangle$ is replaced by $\langle \widehat{\mathcal{W}}_\alpha \widehat{\mathcal{W}}_\beta^\star \rangle$, where the star denotes a complex conjugate (more generally, we denote an adjoint of a matrix or linear operator with a star). We recall that we take the temperature T to be spatially constant.

It is important to emphasize here that the nonlinear fluctuating NS equations, with the white-noise stochastic forcing terms (9), are ill-defined because the solution should be a distribution rather than a function and the nonlinear terms cannot be interpreted in the sense of distributions. The nonlinear equations can be interpreted using a small-scale *regularization* (smoothing) of the stochastic forcing, along with a suitable renormalization of the transport coefficients [11, 58]. Such a regularization is naturally provided by the discretization or coarse-graining [57] length scale. As

long as there are sufficiently many molecules per hydrodynamic cell, the fluctuations will be small and the behavior of the nonlinear equations will closely follow that of the *linearized* equations of fluctuating hydrodynamics, which can be given a precise meaning [59]. This can be checked by reducing ϵ to the point where the observed spatio-temporal correlations of the fluctuations begin to scale linearly with ϵ, indicating that nonlinear effects are negligible. In all of the simulations reported here, we have used $\epsilon = 1$ but have checked that using a very small ϵ and then rescaling the covariance of the fluctuations by ϵ^{-1} gives indistinguishable results to within statistical errors.

Note that for the linearized equations the noise is additive since the covariance of the stochastic forcing terms is to be evaluated at the mean around which the linearization is performed. That is, in the linearized equations ($\epsilon \to 0$) one should read (11) as $\boldsymbol{\Psi} = \sqrt{2\chi\rho M\, \bar{c}(1-\bar{c})}\, \boldsymbol{\mathcal{W}}_c$, where $\bar{c}$ is the solution of the deterministic equations. Therefore, there is no Itô–Stratonovich difficulty in interpreting the stochastic terms, and we use the (ambiguous) "Langevin" notation that is standard in the physics literature, instead of the differential notation more common in the literature on SDEs.

It is important to observe that even when linearized, (6)–(8) is a very challenging system of multiscale equations. Even a single stochastic advection-diffusion equation such as (7) is inherently multiscale because thermal fluctuations span the whole range of spatio-temporal scales from the microscopic to the macroscopic; specifically, *all* modes of the spatial discretization have a nontrivial stochastic dynamics that must be reproduced by the numerical method. Including the density equation (6) in the system of equations leads to fast sound wave modes that make the compressible equations stiff even in the deterministic setting. Finally, in most applications of interest the concentration diffusion is much slower than the momentum diffusion, leading to additional stiffness and multiscale nature of the equations, as we discuss further in section 5.

2.1. Incompressible equations. If density variations are negligible, $\rho = \rho_0 =$ const, we obtain the *incompressible* approximation to the hydrodynamic equations (6)–(8) [17],

$$\begin{aligned} \partial_t \boldsymbol{v} &= -\boldsymbol{\nabla}\pi - \boldsymbol{\nabla}\cdot\left(\boldsymbol{v}\boldsymbol{v}^T\right) + \nu\boldsymbol{\nabla}^2\boldsymbol{v} + \rho^{-1}\boldsymbol{f}_v \\ &= \boldsymbol{\mathcal{P}}\left[-\boldsymbol{v}\cdot\boldsymbol{\nabla}\boldsymbol{v} + \nu\boldsymbol{\nabla}^2\boldsymbol{v} + \rho^{-1}\boldsymbol{f}_v\right], \end{aligned} \tag{14}$$

$$\partial_t c = -\boldsymbol{\nabla}\cdot\left[c\,(\boldsymbol{v}-\boldsymbol{v}_s)\right] + \chi\boldsymbol{\nabla}^2 c + \rho^{-1} f_c, \tag{15}$$

where $\nu = \eta/\rho$, and $\boldsymbol{v}\cdot\boldsymbol{\nabla}c = \boldsymbol{\nabla}\cdot(c\boldsymbol{v})$ and $\boldsymbol{v}\cdot\boldsymbol{\nabla}\boldsymbol{v} = \boldsymbol{\nabla}\cdot\left(\boldsymbol{v}\boldsymbol{v}^T\right)$ because of the incompressibility constraint $\boldsymbol{\nabla}\cdot\boldsymbol{v} = 0$. Here $\boldsymbol{\mathcal{P}}$ is the orthogonal projection onto the space of divergence-free velocity fields, $\boldsymbol{\mathcal{P}} = \boldsymbol{I} - \boldsymbol{\mathcal{G}}\left(\boldsymbol{\mathcal{D}}\boldsymbol{\mathcal{G}}\right)^{-1}\boldsymbol{\mathcal{D}}$ in real space, where $\boldsymbol{\mathcal{D}}\square \equiv \boldsymbol{\nabla}\cdot\square$ denotes the divergence operator and $\boldsymbol{\mathcal{G}} \equiv \boldsymbol{\nabla}$ the gradient operator. With periodic boundaries we can express all operators in Fourier space and $\widehat{\boldsymbol{\mathcal{P}}} = \boldsymbol{I} - k^{-2}(\boldsymbol{k}\boldsymbol{k}^\star)$, where $\boldsymbol{k}$ is the wavenumber.

Fluctuations can be included in the incompressible equations via the stochastic forcing terms

$$\begin{aligned} \rho^{-1}\boldsymbol{f}_v &= \rho^{-1}\epsilon^{\frac{1}{2}}\boldsymbol{\nabla}\cdot\boldsymbol{\Sigma}_s = \boldsymbol{\nabla}\cdot\left(\sqrt{2\epsilon\nu\rho^{-1}k_BT}\,\widetilde{\boldsymbol{\mathcal{W}}}_{\boldsymbol{v}}\right), \\ \rho^{-1}f_c &= \rho^{-1}\epsilon^{\frac{1}{2}}\boldsymbol{\nabla}\cdot\boldsymbol{\Psi} = \boldsymbol{\nabla}\cdot\left[\sqrt{2\epsilon\chi\rho^{-1}M\,c(1-c)}\,\boldsymbol{\mathcal{W}}_c\right]. \end{aligned}$$

Note that it is not necessary to include the stochastic pressure fluctuations $\boldsymbol{\Sigma}_p$ in (10) in the incompressible velocity equation (14) since the projection eliminates any

nonzero trace component of the stress tensor. In our formulation, we use a strictly symmetric stochastic stress tensor $\boldsymbol{\Sigma}_s$ in the incompressible equations. This is based on physical arguments about local angular momentum conservation [60, 61]. At the same time, the only thing that matters in the Fokker–Planck description is the covariance of the stochastic forcing in the velocity equation $\boldsymbol{\mathcal{P}}\boldsymbol{\mathcal{D}}\boldsymbol{\Sigma}_s$. This covariance is determined from the fluctuation dissipation balance principle,

$$\left\langle \left(\boldsymbol{\mathcal{P}}\boldsymbol{\mathcal{D}}\boldsymbol{\Sigma}_s\right)\left(\boldsymbol{\mathcal{P}}\boldsymbol{\mathcal{D}}\boldsymbol{\Sigma}_s\right)^{\star}\right\rangle = \boldsymbol{\mathcal{P}}\boldsymbol{\mathcal{D}}\left\langle \boldsymbol{\Sigma}_s\boldsymbol{\Sigma}_s^{\star}\right\rangle \boldsymbol{\mathcal{D}}\boldsymbol{\mathcal{P}} = \boldsymbol{\mathcal{P}}\boldsymbol{\mathcal{L}}\boldsymbol{\mathcal{P}}, \tag{16}$$

where $\boldsymbol{\mathcal{L}}$ is the vector Laplacian operator. Because $\boldsymbol{\mathcal{P}}$ and $\boldsymbol{\mathcal{D}}$ have nontrivial null spaces, (16) does not uniquely determine the covariance of the stochastic stress. In fact, it can easily be shown by going to the Fourier domain that one can have a nonsymmetric component to the stochastic stress without violating (16). We believe that the stress tensor should be symmetric since we do not include an additional equation for the intrinsic spin (angular momentum) density. This is appropriate for fluids composed of "point" particles; however, recent molecular dynamics simulations have shown that for molecular liquids there can be nontrivial coupling between the linear and spin momentum densities [61]. While spin density has been included in the fluctuating hydrodynamics equations [60] at the theoretical level, we are not aware of any numerical simulations of such equations and do not consider an angular momentum equation in this work.

2.2. Steady-state covariances. The means and spatio-temporal covariances of the fluctuating fields fully characterize the Gaussian solution of the linearized equations [28]. Of particular importance is the steady-state covariance of the fluctuating fields, which can be obtained for periodic systems by linearizing the equations in the fluctuations and using a spatial Fourier transform to decouple the different modes (wavevectors $\boldsymbol{k}$). This steady-state covariance in Fourier space is usually referred to as a *static structure factor* in the physical literature and represents the covariance matrix of the Fourier spectra of a typical snapshot of the fluctuating fields. Note that it is in principle possible to calculate the covariance of the fluctuations in nonperiodic domains as well [62]; however, these tedious calculations offer little additional physical insight over the simple results presented below. We will present numerical algorithms that can solve the fluctuating equations with nonperiodic boundary conditions; however, periodic conditions will be used to test the accuracy of the spatio-temporal discretization by comparing to the simple theory.

At thermodynamic equilibrium, the fluctuations of the different hydrodynamic variables are uncorrelated and white in space, that is, the equilibrium variance is independent of the wavevector $\boldsymbol{k}$ [28], in agreement with equilibrium statistical mechanics [16, 63]. Consider first the fluctuating isothermal compressible NS equations (6)–(8) linearized around a uniform steady state, $(\rho, \boldsymbol{v}, c) = (\rho_0 + \delta\rho, \boldsymbol{v}_0 + \delta\boldsymbol{v}, c_0 + \delta c)$, $T = T_0$. Because of Galilean invariance, the advective terms $\boldsymbol{v}_0 \cdot \boldsymbol{\nabla}(\square)$ due to the presence of a background flow do not affect the equilibrium covariances (structure factors), which are found to be [17, 28]

$$\begin{aligned} S_{\rho,\rho} &= \left\langle \left(\widehat{\delta\rho}\right)\left(\widehat{\delta\rho}\right)^{\star}\right\rangle = \rho_0 k_B T_0 / c_T^2, \\ \boldsymbol{S}_{\boldsymbol{v},\boldsymbol{v}} &= \left\langle (\widehat{\delta\boldsymbol{v}})(\widehat{\delta\boldsymbol{v}})^{\star}\right\rangle = \rho_0^{-1} k_B T_0\, \boldsymbol{I}, \\ S_{c,c} &= \left\langle \left(\widehat{\delta c}\right)\left(\widehat{\delta c}\right)^{\star}\right\rangle = M\rho_0^{-1}\, c_0(1-c_0). \end{aligned} \tag{17}$$

At equilibrium, there are no cross-correlations between the different variables, for example, $\boldsymbol{S}_{c,\boldsymbol{v}} = \langle(\widehat{\delta c})(\widehat{\delta \boldsymbol{v}})^\star\rangle = \boldsymbol{0}$. The equilibrium variance of the spatial average of a given variable over a cell of volume ΔV can be obtained by dividing the corresponding structure factor by ΔV; for example, the variance of the concentration is $\left\langle (\delta\rho)^2 \right\rangle = \rho_0 k_B T_0 / \left(c_T^2 \Delta V\right)$. In the incompressible limit, $c_T \to \infty$, the density fluctuations vanish and $\rho \approx \rho_0$.

Out of thermodynamic equilibrium, there may appear long-range correlations between the different hydrodynamic variables [17]. As a prototypical example of such nonequilibrium fluctuations, we focus on the incompressible equations (14)–(15) in the presence of an imposed concentration gradient $\boldsymbol{\nabla}\bar{c}$. The spatial nonuniformity of the mean concentration when there is a gradient breaks the translational symmetry, and the Fourier transform no longer diagonalizes the equations. We focus our analysis and test our numerical schemes on a periodic approximation in which we linearize around a uniform background state $(\boldsymbol{v}, c) = (\delta\boldsymbol{v},\ c_0 + \delta c)$, as suggested and justified in the physics literature on long-range nonequilibrium correlations [17, 38, 39, 45]. In such a periodic approximation we cannot have a gradient in the steady-state average concentration c_0, but we can mimic the effect of the advective term $\boldsymbol{v} \cdot \boldsymbol{\nabla} c_0$ with an additional term $\boldsymbol{v} \cdot (\boldsymbol{\nabla}\bar{c})$ in the concentration equation. This is justified if the concentration gradient is weak and leads to the linearized equations in a periodic domain

$$
\begin{aligned}
\partial_t\left(\delta\boldsymbol{v}\right) &= \boldsymbol{\mathcal{P}}\left[\nu\boldsymbol{\nabla}^2\left(\delta\boldsymbol{v}\right) + \boldsymbol{\nabla}\cdot\left(\sqrt{2\nu\rho_0^{-1}k_BT_0}\,\boldsymbol{\mathcal{W}}_{\boldsymbol{v}}\right)\right],\\
\partial_t\left(\delta c\right) &= -\left(\boldsymbol{\nabla}\bar{c}\right)\cdot\left(\delta\boldsymbol{v}\right) + \chi\boldsymbol{\nabla}^2\left(\delta c\right) + \boldsymbol{\nabla}\cdot\left[\sqrt{2\chi\rho_0^{-1}M\,c_0(1-c_0)}\,\boldsymbol{\mathcal{W}}_c\right].
\end{aligned}
\tag{18}
$$

In the Fourier domain (18) is a collection of SDEs, one system of linear additive-noise equations per wavevector $\boldsymbol{k}$, written in differential notation as

$$
\begin{aligned}
d\left(\widehat{\delta\boldsymbol{v}}\right) &= -\nu\,k^2\left(\widehat{\delta\boldsymbol{v}}\right)dt + i\sqrt{2\nu\rho_0^{-1}k_BT_0}\,\widehat{\boldsymbol{\mathcal{P}}}\boldsymbol{k}\cdot\left(d\boldsymbol{\mathcal{B}}_{\boldsymbol{v}}^{(\boldsymbol{k})}\right),\\
d\left(\widehat{\delta c}\right) &= -\left(\boldsymbol{\nabla}\bar{c}\right)\cdot\left(\widehat{\delta\boldsymbol{v}}\right)dt - \chi k^2\left(\widehat{\delta c}\right)dt + i\sqrt{2\chi\rho_0^{-1}M\,c_0(1-c_0)}\,\boldsymbol{k}\cdot\left(d\boldsymbol{\mathcal{B}}_c^{(\boldsymbol{k})}\right),
\end{aligned}
\tag{19}
$$

where we used that $\widehat{\boldsymbol{\mathcal{P}}}(\widehat{\delta\boldsymbol{v}}) = \widehat{\delta\boldsymbol{v}}$. Here $\boldsymbol{\mathcal{B}}_{\boldsymbol{v}}(t)$ is a tensor, and $\boldsymbol{\mathcal{B}}_c(t)$ is a vector, whose components are independent Wiener processes. Note that the velocity equation is not affected by the concentration gradient. Given the model equations (19), the explicit solution for the matrix of static structure factors (covariance matrix)

$$
\boldsymbol{\mathcal{S}} = \begin{bmatrix} \boldsymbol{S}_{\boldsymbol{v},\boldsymbol{v}} & S^\star_{c,\boldsymbol{v}} \\ S_{c,\boldsymbol{v}} & S_{c,c} \end{bmatrix}
$$

can be obtained as the solution of a linear system resulting from the stationarity condition $d\boldsymbol{\mathcal{S}} = \boldsymbol{0}$. For a derivation, see equation (30) in [28] or equation (3.10) in [64] and also (41); below we simply quote the results of these straightforward calculations.

2.2.1. Incompressible velocity fluctuations. By considering the stationarity condition $d\boldsymbol{S}_{\boldsymbol{v},\boldsymbol{v}} = 0$ it can easily be seen that the equilibrium covariance of the velocities is proportional to the projection operator,

$$
\boldsymbol{S}_{\boldsymbol{v},\boldsymbol{v}} = \rho_0^{-1}k_BT_0\,\widehat{\boldsymbol{\mathcal{P}}} = \rho_0^{-1}k_BT_0\,\left[\boldsymbol{I} - k^{-2}(\boldsymbol{k}\boldsymbol{k}^\star)\right],
\tag{20}
$$

independent of the concentration gradient. In particular, the amplitude of the velocity fluctuations at each wavenumber is constant and reduced by one in comparison to the compressible equations,

$$\text{Trace}\, \boldsymbol{S}_{\boldsymbol{v},\boldsymbol{v}} = \left\langle (\widehat{\delta \boldsymbol{v}})^{\star} (\widehat{\delta \boldsymbol{v}}) \right\rangle = (d-1)\, \rho_0^{-1} k_B T_0, \tag{21}$$

where d is the spatial dimension. This is a reflection of the fact that one degree of freedom (i.e., one $k_B T/2$) is subtracted from the kinetic energy due to the incompressibility constraint, which eliminates the sound mode. In Appendix B we generalize (20) to nonperiodic systems, to obtain

$$\left\langle (\delta \boldsymbol{v})\, (\delta \boldsymbol{v})^{\star} \right\rangle = \rho_0^{-1} k_B T_0 \, \left(\Delta V^{-1} \boldsymbol{\mathcal{P}} \right). \tag{22}$$

An alternative way of expressing the result (22) is that all divergence-free modes have the same spectral power at equilibrium. That is, if the fluctuating velocities are expressed in any orthonormal basis for the space of velocities that satisfy $\boldsymbol{\nabla} \cdot \boldsymbol{v} = 0$, at equilibrium the resulting random coefficients should be uncorrelated and have unit variance. This will be useful in section 4.1 for examining the weak accuracy of the spatio-temporal discretizations of the incompressible equations. For periodic boundary conditions, such an orthonormal basis is simple to construct in the Fourier domain and a Fourier transform can be used project the velocity field onto this basis. In particular, for all wavevectors the projection of the velocity fluctuations onto the *longitudinal* mode

$$\hat{\boldsymbol{v}}^{(1)} = k^{-1} \left[k_x,\, k_y,\, k_z \right], \tag{23}$$

where $k = \left(k_x^2 + k_y^2 + k_z^2 \right)^{1/2}$, should be identically zero:

$$\hat{v}_1 = \hat{\boldsymbol{v}}^{(1)} \cdot (\widehat{\delta \boldsymbol{v}}) = \frac{k_x}{k} \widehat{\delta v}_x + \frac{k_y}{k} \widehat{\delta v}_y + \frac{k_z}{k} \widehat{\delta v}_z = k^{-1} \left(\boldsymbol{k} \cdot \widehat{\delta \boldsymbol{v}} \right) = 0.$$

A basis for the incompressible periodic velocity fields can be constructed from the two *vortical* modes

$$\hat{\boldsymbol{v}}^{(2)} = \left(k_x^2 + k_y^2 \right)^{-1/2} \left[-k_y,\, k_x,\, 0 \right], \tag{24}$$

$$\hat{\boldsymbol{v}}^{(3)} = k^{-1} \left(k_x^2 + k_y^2 \right)^{-1/2} \left[k_x k_z,\, k_y k_z,\, -\left(k_x^2 + k_y^2 \right) \right], \tag{25}$$

and the projection of the fluctuating velocities onto these modes has the equilibrium covariance

$$\langle \hat{v}_2 \hat{v}_2^{\star} \rangle = \langle \hat{v}_3 \hat{v}_3^{\star} \rangle = \rho_0^{-1} k_B T_0, \text{ while } \langle \hat{v}_2 \hat{v}_3^{\star} \rangle = 0. \tag{26}$$

In two dimensions only $\hat{\boldsymbol{v}}^{(1)}$ and $\hat{\boldsymbol{v}}^{(2)}$ are present, and $k \hat{\boldsymbol{v}}^{(2)}$ is the z component of the vorticity and spans the subspace of divergence-free velocities. The fact that the $(d-1)$ vortical modes have equal power leads to the velocity variance (21).

2.2.2. Nonequilibrium fluctuations. When a macroscopic concentration gradient is present, the velocity fluctuations affect the concentration via the linearized advective term $(\boldsymbol{\nabla} \bar{c}) \cdot \boldsymbol{v}$. Solving (19) shows an *enhancement* of the concentration fluctuations [65] proportional to the square of the applied gradient,

$$S_{c,c} = M \rho_0^{-1}\, c_0 (1 - c_0) + \frac{k_B T}{\rho \chi (\nu + \chi) k^4} \left(\sin^2 \theta \right) \, (\nabla \bar{c})^2, \tag{27}$$

where θ is the angle between $\boldsymbol{k}$ and $\boldsymbol{\nabla}\bar{c}$, $\sin^2\theta = k_\perp^2/k^2$. Furthermore, there appear *long-range correlations* between the concentration fluctuations and the fluctuations of velocity parallel to the concentration gradient, proportional to the applied gradient [11, 65]:

$$\mathcal{S}_{c,v_\parallel} = \left\langle (\widehat{\delta c})(\widehat{\delta v_\parallel})^\star \right\rangle = -\frac{k_B T}{\rho(\nu+\chi)k^2}\left(\sin^2\theta\right)\,\nabla\bar{c}. \tag{28}$$

The power-law divergence for small k indicates long-range correlations between δc and $\delta\boldsymbol{v}$ and is the cause of the giant fluctuation phenomenon studied in section 5.

3. Spatio-temporal discretization. Designing temporal discretizations for fluid dynamics is challenging even without including thermal fluctuations. When there is no stochastic forcing, our schemes revert to standard second-order discretizations and can be analyzed with existing numerical analysis techniques. Here we tackle the additional goal of constructing discretizations that, in a weak sense, accurately reproduce the statistics of the continuum fluctuations for the linearized equations. Note that achieving second-order weak accuracy is much simpler for linear additive-noise equations since in the linear case the solution is fully characterized by the means and the correlation functions (time-dependent covariances). In fact, one can use any method that is second-order in time in the deterministic setting and also reproduces the correct static (equal-time) covariance to second order, as explained in more detail in [28]. The deterministic order of accuracy can be analyzed using standard techniques, and the accuracy of the static covariances can be analyzed using the techniques described in [28]. We emphasize that the temporal integrators are only higher-order accurate in a weak sense for the linearized equations of fluctuating hydrodynamics [28, 46].

Thermal fluctuations are added to a deterministic scheme as an additional forcing term that represents the temporal average of a stochastic forcing term over the time interval Δt and over the spatial cells of volume ΔV [28]. Because $\boldsymbol{\mathcal{W}}$ is white in space and time, the averaging adds an additional prefactor of $(\Delta V\,\Delta t)^{-1/2}$ in front of the stochastic forcing. In the actual numerical schemes, a "realization" of a white-noise field $\boldsymbol{\mathcal{W}}$ is represented by a collection $\boldsymbol{W}$ of normally distributed random numbers with mean zero and covariance given by (13) or (12), with the identification

$$\boldsymbol{\mathcal{W}} \longleftrightarrow (\Delta V\,\Delta t)^{-1/2}\,\boldsymbol{W}.$$

Specifically, the stochastic fluxes (10) are discretized as

$$\boldsymbol{\Sigma}_s = \sqrt{\frac{2\eta k_B T}{\Delta V\,\Delta t}}\,\widetilde{\boldsymbol{W}}_{\boldsymbol{v}} \quad \text{and} \quad \boldsymbol{\Psi} = \sqrt{\frac{2\chi\rho M\,c(1-c)}{\Delta V\,\Delta t}}\,\boldsymbol{W}_c. \tag{29}$$

A realization of $\boldsymbol{W}$ is sampled using a pseudorandom number stream. The temporal discretization of the stochastic forcing corresponds to the choice of how many realizations of $\boldsymbol{W}$ are generated per time step and how each realization is associated with specific points in time inside a time step (e.g., the beginning, midpoint, or endpoint of a time step). The spatial discretization corresponds to the choice of how many normal variates to generate per spatial cell and how to associate them with elements of the spatial discretization (e.g., cell centers, nodes, faces, or edges). Once these choices are made, it is simple to add the stochastic forcing to an existing deterministic algorithm or code, while still accounting for the fact that white noise is not like a classical smooth forcing and cannot be evaluated pointwise.

3.1. Temporal discretization. As a first step in designing a spatio-temporal discretization for the compressible and incompressible equations of fluctuating hydrodynamics, we focus on the temporal discretization. We assume that the time step is fixed at Δt. The time step index is denoted with a superscript; for example, $\boldsymbol{c}^n$ denotes concentration at time $n\Delta t$, and $\boldsymbol{W}^n$ denotes a realization of $\boldsymbol{W}$ generated at time step n.

In the next section, we will describe our staggered spatial discretization of the crucial differential operators, denoted here rather generically with a letter symbol in order to distinguish them from the corresponding continuum operators. Specifically, let $\boldsymbol{G}$ be the gradient (scalar→vector) operator, $\boldsymbol{D}$ the divergence (vector→scalar) operator, and $\boldsymbol{L} = \boldsymbol{D}\boldsymbol{G}$ the Laplacian (scalar→scalar) operator. When the divergence operator acts on a tensor field $\boldsymbol{F}$ such as a stress tensor $\boldsymbol{\sigma}$, it is understood to act componentwise on the x, y, and z components of the tensor. Similarly, the gradient and Laplacian operators act componentwise on a vector. An important property of the discrete operators that we require to hold is that the divergence operator is the negative adjoint of the gradient, $\boldsymbol{D} = -\boldsymbol{G}^\star$. This ensures that the scheme satisfies a discrete version of the continuous property

$$\int_\Omega w\,[\boldsymbol{\nabla}\cdot\boldsymbol{v}]\;d\boldsymbol{r} = -\int_\Omega \boldsymbol{v}\cdot\boldsymbol{\nabla} w\,d\boldsymbol{r} \text{ if } \boldsymbol{v}\cdot\boldsymbol{n}_{\partial\Omega} = 0 \text{ or } \boldsymbol{v} \text{ is periodic}$$

for any scalar field $w(\boldsymbol{r})$.

We define the weak order of accuracy of a temporal discretization in terms of the mismatch between the steady-state covariance of the continuum and the discrete formulations. With periodic boundary conditions this would be the mismatch between the Fourier spectrum of a typical snapshot of the true solution and the steady-state discrete spectrum of the numerical solution [28]. This mismatch is typically of the form $O(\Delta t^k)$ for some integer $k \geq 1$, implying that for sufficiently small time steps the discrete formulation reproduces the steady-state covariance of the continuum formulation. Note that for the linearized equations a certain order of deterministic temporal accuracy, combined with equal or higher order of accuracy of the steady-state covariances, implies the same order of accuracy for all temporal correlations. A theoretical analysis of the weak accuracy of the temporal discretizations used in this work can be performed using the tools described in [28] with some straightforward extensions [46]; here we simply state the main results and verify the order of weak accuracy numerically.

3.1.1. Compressible equations. With $\boldsymbol{Q} = (\rho, \boldsymbol{v}, c)$ denoting the fluctuating field, the fluctuating compressible NS equations (6)–(8) can be written as a general stochastic conservation law,

$$\partial_t \boldsymbol{Q} = -\boldsymbol{D}\left[\boldsymbol{F}(\boldsymbol{Q};t) - \boldsymbol{Z}(\bar{\boldsymbol{Q}}, \boldsymbol{W})\right], \tag{30}$$

where $\boldsymbol{D}$ is the divergence operator (acting componentwise on each flux), $\boldsymbol{F}(\boldsymbol{Q};t)$ is the deterministic flux, and $\boldsymbol{Z} = [0, \boldsymbol{\Sigma}, \boldsymbol{\Psi}]$ is the discretization of the stochastic flux (29). We recall that the stochastic forcing amplitude is written as multiplicative in the state; however, in the linearized limit of weak fluctuations the strength of the stochastic forcing depends only on the *mean* state, which is well-approximated by the instantaneous state, $\bar{\boldsymbol{Q}}(t) \approx \boldsymbol{Q}(t)$. Following [29], we base our temporal discretization of (30) on the (optimal) three-stage low-storage strong stability preserving [66] (originally called total variation diminishing [67]) Runge–Kutta (RK3) scheme of Gottlieb

and Shu, ensuring stability in the inviscid limit without requiring slope-limiting. The stochastic terms are discretized using two random fluxes per time step, as proposed in [28]. This discretization achieves third-order weak accuracy [46] for linear additive-noise equations, while requiring only the generation of two Gaussian random fields per time step.

For each stage of our third-order Runge–Kutta scheme, a conservative increment is calculated as

$$\Delta \boldsymbol{Q}(\boldsymbol{Q}, \boldsymbol{W}; t) = -\Delta t\, \boldsymbol{DF}(\boldsymbol{Q};\, t) + \Delta t\, \boldsymbol{DZ}(\boldsymbol{Q}, \boldsymbol{W}).$$

Each time step of the RK3 algorithm is composed of three stages, the first one estimating $\boldsymbol{Q}$ at time $t = (n+1)\Delta t$, the second at $t = (n+\frac{1}{2})\Delta t$, and the final stage obtaining a third-order accurate estimate at $t = (n+1)\Delta t$. Each stage consists of an Euler–Maruyama step followed by a weighted averaging with the value from the previous stage,

$$\begin{aligned}
\widetilde{\boldsymbol{Q}}^{n+1} &= \boldsymbol{Q}^n + \Delta \boldsymbol{Q}\left(\boldsymbol{Q}^n, \boldsymbol{W}_1^n\,;\, n\Delta t\right), \\
\widetilde{\boldsymbol{Q}}^{n+\frac{1}{2}} &= \frac{3}{4}\boldsymbol{Q}^n + \frac{1}{4}\left[\widetilde{\boldsymbol{Q}}^{n+1} + \Delta \boldsymbol{Q}\left(\widetilde{\boldsymbol{Q}}^{n+1}, \boldsymbol{W}_2^n\,;\, (n+1)\Delta t\right)\right], \\
\boldsymbol{Q}^{n+1} &= \frac{1}{3}\boldsymbol{Q}^n + \frac{2}{3}\left[\widetilde{\boldsymbol{Q}}^{n+\frac{1}{2}} + \Delta \boldsymbol{Q}\left(\widetilde{\boldsymbol{Q}}^{n+\frac{1}{2}}, \boldsymbol{W}_3^n\,;\, (n+\frac{1}{2})\Delta t\right)\right],
\end{aligned} \tag{31}$$

where the stochastic fluxes between different stages are related to each other via

$$\begin{aligned}
\boldsymbol{W}_1^n &= \boldsymbol{W}_A^n + w_1 \boldsymbol{W}_B^n, \\
\boldsymbol{W}_2^n &= \boldsymbol{W}_A^n + w_2 \boldsymbol{W}_B^n, \\
\boldsymbol{W}_3^n &= \boldsymbol{W}_A^n + w_3 \boldsymbol{W}_B^n,
\end{aligned} \tag{32}$$

and $\boldsymbol{W}_A^n$ and $\boldsymbol{W}_B^n$ are two independent realizations of $\boldsymbol{W}$ that are generated independently at each RK3 step. In this work we used the weights derived in [28] based on a linearized analysis, $w_1 = -\sqrt{3}$, $w_2 = \sqrt{3}$, and $w_3 = 0$. More recent analysis based on the work in [68] shows that second-order weak accuracy is achieved for additive-noise *nonlinear* SDEs using the weights [46]

$$w_1 = \frac{\left(2\sqrt{2} \mp \sqrt{3}\right)}{5}, \quad w_2 = \frac{\left(-4\sqrt{2} \mp 3\sqrt{3}\right)}{5}, \quad w_3 = \frac{\left(\sqrt{2} \pm 2\sqrt{3}\right)}{10}.$$

For the types of problems studied here, nonlinearities play a minimal role and either choice of the weights is appropriate.

3.1.2. Incompressible equations. The spatially discretized equations (14)–(15) can be written in the form

$$\begin{aligned}
\partial_t \boldsymbol{v} + \boldsymbol{G}\pi &= \boldsymbol{A}_{\boldsymbol{v}}(\boldsymbol{v}, c) + \nu \boldsymbol{L}\boldsymbol{v} + \rho^{-1}\boldsymbol{f}_v, \\
\partial_t c &= \boldsymbol{A}_c(\boldsymbol{v}, c) + \chi \boldsymbol{L} c + \rho^{-1} f_c, \\
\boldsymbol{D}\boldsymbol{v} &= \boldsymbol{0},
\end{aligned}$$

where $\boldsymbol{A}(\boldsymbol{v}, c)$ represent the nondiffusive deterministic terms, such as the advective and Soret forcing terms, as well as any additional terms arising from gravity or other

effects. Fluctuations are accounted for via the stochastic forcing terms

$$\rho^{-1}\boldsymbol{f}_v\left(\widetilde{\boldsymbol{W}}_{\boldsymbol{v}}\right)=\boldsymbol{D}\left[\sqrt{\frac{2\epsilon\nu\rho^{-1}k_BT}{\Delta V\,\Delta t}}\,\widetilde{\boldsymbol{W}}_{\boldsymbol{v}}\right],$$
$$\rho^{-1}f_c\left(c,\boldsymbol{W}_c\right)=\boldsymbol{D}\left[\sqrt{\frac{2\epsilon\chi\rho^{-1}M\;c(1-c)}{\Delta V\,\Delta t}}\,\boldsymbol{W}_c\right].$$

We base our temporal discretization on the second-order semi-implicit deterministic scheme of Griffith [34], a predictor-corrector method in which the predictor step combines the Crank–Nicolson method for the diffusive terms with the Euler method for the remaining terms

$$\begin{aligned}\frac{\tilde{\boldsymbol{v}}^{n+1}-\boldsymbol{v}^n}{\Delta t}+\boldsymbol{G}\tilde{\pi}^{n+\frac{1}{2}}&=\boldsymbol{A}_{\boldsymbol{v}}(\boldsymbol{v}^n,c^n)+\nu\boldsymbol{L}\left(\frac{\tilde{\boldsymbol{v}}^{n+1}+\boldsymbol{v}^n}{2}\right)+\rho^{-1}\boldsymbol{f}_v\left(\widetilde{\boldsymbol{W}}_{\boldsymbol{v}}^n\right),\\ \frac{\tilde{c}^{n+1}-c^n}{\Delta t}&=\boldsymbol{A}_c(\boldsymbol{v}^n,c^n)+\chi\boldsymbol{L}\left(\frac{\tilde{c}^{n+1}+c^n}{2}\right)+\rho^{-1}f_c\left(c^n,\boldsymbol{W}_c^n\right),\\ \boldsymbol{D}\tilde{\boldsymbol{v}}^{n+1}&=\boldsymbol{0}.\end{aligned}\tag{33}$$

The corrector stage combines Crank–Nicolson for the diffusive terms with an explicit second-order approximation for the remaining deterministic terms

$$\begin{aligned}\frac{\boldsymbol{v}^{n+1}-\boldsymbol{v}^n}{\Delta t}+\boldsymbol{G}\pi^{n+\frac{1}{2}}&=\boldsymbol{A}_{\boldsymbol{v}}^{n+\frac{1}{2}}+\nu\boldsymbol{L}\left(\frac{\boldsymbol{v}^{n+1}+\boldsymbol{v}^n}{2}\right)+\rho^{-1}\boldsymbol{f}_v^{n+\frac{1}{2}},\\ \frac{c^{n+1}-c^n}{\Delta t}&=\boldsymbol{A}_c^{n+\frac{1}{2}}+\chi\boldsymbol{L}\left(\frac{c^{n+1}+c^n}{2}\right)+\rho^{-1}f_c^{n+\frac{1}{2}},\\ \boldsymbol{D}\boldsymbol{v}^{n+1}&=\boldsymbol{0}.\end{aligned}\tag{34}$$

Unlike a fractional-step scheme that splits the velocity and pressure updates [69, 70], this approach simultaneously solves for the velocity and pressure and avoids the need to determine appropriate "intermediate" boundary conditions. Importantly, no spurious boundary modes [71, 72] arise due to the implicit velocity treatment even in the presence of physical boundaries, which is especially important for fluctuating hydrodynamics since all of the modes are stochastically forced [46].

The concentration equation in (34) (and similarly in (33)) is a linear system for c^{n+1} that appears in standard semi-implicit discretizations of diffusion and is solved using a standard multigrid method. The velocity equation in (34) (and similarly in (33)) is a much harder "saddle-point" system of linear equations to be solved for the variables $\boldsymbol{v}^{n+1}$ and $\pi^{n+\frac{1}{2}}$. This time-dependent Stokes problem is solved using a Krylov iterative solver as described in detail in [34]. The ill-conditioning of the Stokes system is mitigated by using a projection method (an inhomogeneous Helmholtz solve for velocity followed by a Poisson solve for the pressure) as a preconditioner. With periodic boundary conditions, solving the Stokes system is equivalent to a projection method, that is, to an unconstrained step for the velocities followed by an application of the projection operator. If physical boundaries are present, then the projection method is only an approximate solver for the incompressible Stokes equations; however, the "splitting error" incurred by the approximations inherent in the projection method is corrected by the Krylov solver.

The nonlinear terms are approximated in the corrector stage using an *explicit trapezoidal rule*,

$$\boldsymbol{A}_{\boldsymbol{v}}^{n+\frac{1}{2}} = \frac{1}{2}\left[\boldsymbol{A}_{\boldsymbol{v}}(\boldsymbol{v}^n, c^n) + \boldsymbol{A}_{\boldsymbol{v}}(\tilde{\boldsymbol{v}}^{n+1}, \tilde{c}^{n+1})\right], \tag{35}$$

which is the (optimal) two-stage strong stability preserving Runge–Kutta method [66] and is thus generally preferable for hyperbolic conservation laws. For the stochastic forcing terms, we employ a temporal discretization that uses one random flux per time step,

$$\boldsymbol{f}_v^{n+\frac{1}{2}} = \boldsymbol{f}_v\left(\widetilde{\boldsymbol{W}}_{\boldsymbol{v}}^n\right) \quad \text{and} \quad f_c^{n+\frac{1}{2}} = f_c\left(\tilde{c}^{n+\frac{1}{2}}, \boldsymbol{W}_c^n\right),$$

where $\tilde{c}^{n+\frac{1}{2}} = \left(c^n + \tilde{c}^{n+1}\right)/2$, but we again emphasize that the dependence of $f_c^{n+\frac{1}{2}}$ on the instantaneous state $\tilde{c}^{n+\frac{1}{2}}$ is not important in the weak-noise (linearized) setting. It can be shown that this temporal discretization is second-order weakly accurate for additive-noise nonlinear SDEs [46]. More importantly, the Crank–Nicolson method balances the numerical dissipation with the stochastic forcing *identically* in the linear setting. This important property allows our time stepping to underresolve the fast dynamics of the small-wavelength fluctuations while still maintaining the correct spectrum for the fluctuations at all scales. While this surprising fact has already been verified (in a simplified setting) in the appendix of [28] and also in [73], we give a different derivation in Appendix A. A more detailed analysis will be presented in a forthcoming paper [46].

The *linearized* equations (18) have additional structure that enables us to simplify the predictor algorithm. First, the momentum equation is independent of the concentration equation(s), $\boldsymbol{A}_{\boldsymbol{v}}(\boldsymbol{v}, c) = \boldsymbol{0}$, and the corrector step of the velocity equation is redundant since it simply repeats the predictor step, $\tilde{\boldsymbol{v}}^{n+1} = \boldsymbol{v}^{n+1}$. Therefore, we need only do one Stokes solve per time step. Furthermore, only velocity enters the linearized concentration equation, $\boldsymbol{A}_c(\boldsymbol{v}, c) = \widetilde{\boldsymbol{A}}\boldsymbol{v}$, and therefore

$$\boldsymbol{A}_c^{n+\frac{1}{2}} = \widetilde{\boldsymbol{A}}\tilde{\boldsymbol{v}}^{n+\frac{1}{2}} = \widetilde{\boldsymbol{A}}\frac{\left(\boldsymbol{v}^n + \boldsymbol{v}^{n+1}\right)}{2} = \widetilde{\boldsymbol{A}}\boldsymbol{v}^{n+\frac{1}{2}}$$

can be calculated without performing a predictor step for the concentration. This variation of the time stepping is twice as efficient and can be thought of as a *split* algorithm in which we first do a Crank–Nicolson step for the velocity equation,

$$\frac{\boldsymbol{v}^{n+1} - \boldsymbol{v}^n}{\Delta t} + \boldsymbol{G}\pi^{n+\frac{1}{2}} = \nu\boldsymbol{L}\left(\frac{\boldsymbol{v}^{n+1} + \boldsymbol{v}^n}{2}\right) + \rho^{-1}\boldsymbol{f}_v\left(\widetilde{\boldsymbol{W}}_{\boldsymbol{v}}^n\right), \tag{36}$$

and then a Crank–Nicolson step for the concentration equation using the midpoint velocity to calculate advective fluxes:

$$\frac{c^{n+1} - c^n}{\Delta t} = \widetilde{\boldsymbol{A}}\left(\frac{\boldsymbol{v}^{n+1} + \boldsymbol{v}^n}{2}\right) + \chi\boldsymbol{L}\left(\frac{c^{n+1} + c^n}{2}\right) + \rho^{-1}f_c\left(c^n, \boldsymbol{W}_c^n\right). \tag{37}$$

Because of the special structure of the equations, the split algorithm is equivalent to the traditional Crank–Nicolson method applied to the *coupled* velocity-concentration system, in which both advection and diffusion are treated semi-implicitly. This observation, together with the derivation in Appendix A, shows that the split scheme gives the correct steady-state covariances for *any time step* size Δt, although it does not reproduce the correct dynamics for large Δt. This property will prove very useful for the simulations of giant fluctuations reported in section 5.

3.2. Spatial discretization. We now consider spatial discretization of the equations of fluctuating hydrodynamics on a regular Cartesian grid, focusing on two dimensions for notational simplicity. The spatial discretization is to be interpreted in the finite-volume sense; that is, the value of a fluctuating field at the center of a spatial cell of volume ΔV represents the average value of the fluctuating field over the cell. We explicitly enforce strict local conservation by using a conservative discretization of the divergence. Specifically, the change of the average value inside a cell can always be expressed as a sum of fluxes through each of the faces of the cell, even if we do not explicitly write it in that form.

Consider at first a simplified form of the stochastic advection-diffusion equation for a scalar concentration field

$$\partial_t c = \boldsymbol{\nabla} \cdot \left[-c\boldsymbol{v} + \chi \boldsymbol{\nabla} c + \sqrt{2\chi}\, \boldsymbol{\mathcal{W}}_c \right], \tag{38}$$

where $\boldsymbol{v}(\boldsymbol{r}, t)$ is a given advection velocity. We note that for incompressible flow, we can split the stochastic stress tensor $\boldsymbol{W}_v$ into a vector $\boldsymbol{W}_x$ corresponding to the flux for $\boldsymbol{v}_x$ and a vector $\boldsymbol{W}_y$ corresponding to $\boldsymbol{v}_y$. We can then view the velocity equation as a constrained pair of stochastic advection-diffusion equations of the form (38), one equation for $\boldsymbol{v}_x$ and another for $\boldsymbol{v}_y$. We will discuss the generalization to compressible flow in section 3.2.5.

The spatial discretization described in this section is to be combined with a suitable stable temporal discretization; specifically, the temporal discretization that we employ was described in section 3.1. We consider here the limit of small time steps, $\Delta t \to 0$, corresponding formally to a semidiscrete "method of lines" spatial discretization of the form

$$\frac{d\boldsymbol{c}}{dt} = \boldsymbol{D} \left[(-\boldsymbol{U}\boldsymbol{c} + \chi \boldsymbol{G}\boldsymbol{c}) + \sqrt{2\chi / (\Delta V\, \Delta t)}\, \boldsymbol{W}_c \right], \tag{39}$$

where $\boldsymbol{c} = \{c_{i,j}\}$ is a finite-volume representation of the random field $c(\boldsymbol{r}, t)$. Here, $\boldsymbol{D}$ is a conservative discrete divergence, $\boldsymbol{G}$ is a discrete gradient, $\boldsymbol{U} \equiv \boldsymbol{U}(\boldsymbol{v})$ denotes a discretization of advection by the spatially discrete velocity field $\boldsymbol{v}$, and $\boldsymbol{W}_c$ denotes a vector of normal variates with specified covariance $\boldsymbol{C}_{\boldsymbol{W}} = \langle \boldsymbol{W}_c \boldsymbol{W}_c^{\star} \rangle$.

3.2.1. Discrete fluctuation-dissipation balance. We judge the weak accuracy of the spatial discretization by comparing the steady-state covariance of the spatially discrete fields to the theoretical covariance of the continuum fields in the limit $\Delta t \to 0$ [28]. Ignoring for a moment constraints such as incompressibility, at thermodynamic equilibrium the variance of the discrete fields should be inversely proportional to ΔV and values in distinct cells should be uncorrelated:

$$\boldsymbol{C}_{\boldsymbol{c}} = \langle \boldsymbol{c}\boldsymbol{c}^{\star} \rangle = S_{c,c} \left(\Delta V^{-1} \boldsymbol{I} \right). \tag{40}$$

For periodic systems, this means that the spectral power of each discrete Fourier mode should be equal to the continuum structure factor, $S_{c,c} = 1$ for the model equation (38) (see also (17)), independent of the wavenumber.

A spatial discretization that gives the correct equilibrium discrete covariance is said to satisfy the *discrete fluctuation-dissipation balance* (DFDB) condition [28, 46]. The condition guarantees that for sufficiently small time steps the statistics of the discrete fluctuations are consistent with the continuum formulation. For larger time steps, the difference between the discrete and continuum covariances will depend on the order of weak accuracy of the temporal discretization [74]. A simple way to obtain

the DFDB condition is from the time stationarity of the covariance. For the model equation (38), we obtain the linear system of equations for the matrix $\boldsymbol{C_c}$,

$$\frac{d\boldsymbol{C_c}}{dt} = \boldsymbol{D}\left(-\boldsymbol{U} + \chi\boldsymbol{G}\right)\boldsymbol{C_c} + \boldsymbol{C_c}\left[\boldsymbol{D}\left(-\boldsymbol{U} + \chi\boldsymbol{G}\right)\right]^\star + 2\chi\Delta V^{-1}\boldsymbol{D}\boldsymbol{C_W}\boldsymbol{D}^\star = \boldsymbol{0}, \tag{41}$$

whose solution we would like to be given by (40), specifically, $\boldsymbol{C_c} = \Delta V^{-1}\boldsymbol{I}$. Considering first the case of no advection, $\boldsymbol{U} = \boldsymbol{0}$, we obtain the DFDB condition

$$\boldsymbol{D}\boldsymbol{G} + (\boldsymbol{D}\boldsymbol{G})^\star = -2\boldsymbol{D}\boldsymbol{C_W}\boldsymbol{D}^\star. \tag{42}$$

Consider first the case of periodic boundary conditions. A straightforward way to ensure the condition (42) is to take the components of the random flux $\boldsymbol{W}_c$ to be uncorrelated normal variates with mean zero and unit variance, $\boldsymbol{C_W} = \boldsymbol{I}$, and to also choose the discrete divergence and gradient operators to be negative adjoints of each other, $\boldsymbol{G} = -\boldsymbol{D}^\star$, just as the continuum operators are [25, 28, 64] (see (43)). Alternative approaches and the advantages of the above "random flux" approach are discussed in [64]. As we will demonstrate numerically in section 4, the staggered discretization of the dissipative and stochastic terms described below satisfies the DFDB condition for both compressible flow and incompressible flow.

In the continuum equation (38), the advective term does not affect the fluctuation-dissipation balance at equilibrium; advection simply transports fluctuations without dissipating or amplifying them. This follows from the skew-adjoint property

$$\int_\Omega w\left[\boldsymbol{\nabla}\cdot(c\boldsymbol{v})\right]d\boldsymbol{r} = -\int_\Omega c\left[\boldsymbol{\nabla}\cdot(w\boldsymbol{v})\right]d\boldsymbol{r} \text{ if } \boldsymbol{\nabla}\cdot\boldsymbol{v} = 0 \text{ and } \boldsymbol{v}\cdot\boldsymbol{n}_{\partial\Omega} = 0 \text{ or } \boldsymbol{v} \text{ is periodic}, \tag{43}$$

which holds for any scalar field $w(\boldsymbol{r})$. In particular, choosing $w \equiv c$ shows that for an advection equation $\partial_t c = -\boldsymbol{\nabla}\cdot(c\boldsymbol{v})$ the "energy" $\int c^2\,d\boldsymbol{r}/2$ is a conserved quantity. To ensure that the DFDB condition (41) is satisfied, the matrix $\boldsymbol{D}\boldsymbol{U}\boldsymbol{C_c}$, or, more precisely, the discrete advection operator $\boldsymbol{S} = \boldsymbol{D}\boldsymbol{U}$, should be skew-adjoint, $\boldsymbol{S}^\star = -\boldsymbol{S}$. Specifically, denoting with $\boldsymbol{c}\cdot\boldsymbol{w} = \sum_{i,j} c_{i,j}w_{i,j}$ the discrete dot product, we require that for all $\boldsymbol{w}$

$$\boldsymbol{w}\cdot\left[(\boldsymbol{D}\boldsymbol{U})\,\boldsymbol{c}\right] = -\boldsymbol{c}\cdot\left[(\boldsymbol{D}\boldsymbol{U})\,\boldsymbol{w}\right] \tag{44}$$

if the advection velocities are discretely divergence free, $(\boldsymbol{D}\boldsymbol{U})\,\boldsymbol{1} = \boldsymbol{0}$, where $\boldsymbol{1}$ denotes a vector of all ones. Note that this last condition, $\boldsymbol{S}\boldsymbol{1} = \boldsymbol{0}$, ensures the desirable property that the advection is constant-preserving; that is, advection by the random velocities does not affect a constant concentration field.

For incompressible flow, the additional constraint on the velocity $\boldsymbol{D}\boldsymbol{v} = \boldsymbol{0}$ needs to be taken into account when considering DFDB. In agreement with (22), we require that the equilibrium covariance of the discrete velocities be

$$\langle\boldsymbol{v}\boldsymbol{v}^\star\rangle = \rho_0^{-1}k_BT_0\,\left(\Delta V^{-1}\mathbb{P}\right), \tag{45}$$

where $\mathbb{P}$ is the *discrete projection* operator

$$\mathbb{P} = \boldsymbol{I} - \boldsymbol{G}\left(\boldsymbol{D}\boldsymbol{G}\right)^{-1}\boldsymbol{D} = \boldsymbol{I} - \boldsymbol{D}^\star\left(\boldsymbol{D}\boldsymbol{D}^\star\right)^{-1}\boldsymbol{D}.$$

With periodic boundary conditions, (45) implies that the discrete structure factor for velocity is $S_{\boldsymbol{v},\boldsymbol{v}} = \rho_0^{-1}k_BT_0\,\widehat{\mathbb{P}}$. In particular, the variance of the velocity in each cell is

in agreement with the continuum result since $\operatorname{Tr}\widehat{\mathbb{P}} = \operatorname{Tr}\widehat{\boldsymbol{\mathcal{P}}} = d-1$. More generally, for nonperiodic or nonuniform systems, we require that for sufficiently small time steps all discretely incompressible velocity modes have equal amplitude at equilibrium [46]. In Appendix B we generalize the DFDB condition (42) to the incompressible (constrained) velocity equation and show that there are no additional conditions required from the discrete operators other than the duality condition on the divergence and gradient operators, $\boldsymbol{G} = -\boldsymbol{D}^\star$.

3.2.2. Staggered grid. A cell-centered discretization that is of the form (39) and satisfies the DFDB condition was developed for compressible flow in [28]. Extending this scheme to incompressible flow is, however, nontrivial. In particular, imposing a strict discrete divergence-free condition on collocated velocities has proven to be difficult and is often enforced only approximately [75], which is inconsistent with (45), as we explain in Appendix B. An alternative is to use a staggered grid or "MAC" discretization, as first employed in projection algorithms for incompressible flow [76]. In this discretization, scalars are discretized at cell centers, i.e., placed at points (i, j), while vectors (notably velocities) are discretized on faces of the grid, placing the x component at points $(i + 1/2, j)$ and the y component at $(i, j + 1/2)$. Such a staggered discretization is used for the fluxes in [28], the main difference here being that velocities are also staggered.

In the staggered discretization, the divergence operator maps from vectors to scalars in a locally conservative manner:

$$\boldsymbol{\nabla}\cdot\boldsymbol{v} \to (\boldsymbol{D}\boldsymbol{v})_{i,j} = \Delta x^{-1}\left(v^{(x)}_{i+\frac{1}{2},j} - v^{(x)}_{i-\frac{1}{2},j}\right) + \Delta y^{-1}\left(v^{(y)}_{i,j+\frac{1}{2}} - v^{(y)}_{i,j-\frac{1}{2}}\right).$$

The discrete gradient maps from scalars to vectors, for example, for the x component:

$$(\boldsymbol{\nabla}c)_x \to (\boldsymbol{G}\boldsymbol{c})^{(x)}_{i+\frac{1}{2},j} = \Delta x^{-1}\left(c_{i+1,j} - c_{i,j}\right).$$

It is not hard to show that, with periodic boundary conditions, $\boldsymbol{G} = -\boldsymbol{D}^\star$, as desired. The resulting Laplacian $\boldsymbol{L} = \boldsymbol{D}\boldsymbol{G}$ is the usual 5-point Laplacian,

$$\boldsymbol{\nabla}^2 c \to (\boldsymbol{L}\boldsymbol{c})_{i,j} = \left[\Delta x^{-2}\left(c_{i-1,j} - 2c_{i,j} + c_{i+1,j}\right) + \Delta y^{-2}\left(c_{i,j-1} - 2c_{i,j} + c_{i,j+1}\right)\right],$$

which is negative definite except for the expected trivial translational zero modes. The velocities $\boldsymbol{v}_x$ and $\boldsymbol{v}_y$ can be handled analogously. For example, $\boldsymbol{v}_x$ is represented on its own finite-volume grid, shifted from the concentration (scalar) grid by one half cell along the x axis. The divergence $\boldsymbol{D}^{(x)}$, gradient $\boldsymbol{G}^{(x)}$, and Laplacian $\boldsymbol{L}^{(x)}$ are the same MAC operators as for concentration but shifted to the x-velocity grid.

For the compressible equations, there is an additional dissipative term in (4) that involves $\boldsymbol{\nabla}(\boldsymbol{\nabla}\cdot\boldsymbol{v})$. This term is discretized as written, $\boldsymbol{G}\boldsymbol{D}\boldsymbol{v}$, which can alternatively be expressed in conservative form. When viscosity is spatially dependent, the term $\boldsymbol{\nabla}\cdot\left(\eta\overline{\boldsymbol{\nabla}}\boldsymbol{v}\right)$ should be discretized by calculating a viscous flux on each face of the staggered grids, interpolating viscosity as needed and using the obvious second-order centered differences for each of the terms $\partial_x v_x$, $\partial_x v_y$, $\partial_y v_y$, and $\partial_y v_x$. For a collocated velocity grid, the mixed derivatives $\partial_x v_y$ and $\partial_y v_x$, and the corresponding stochastic forcing terms, do not have an obvious face-centered discretization and require a separate treatment [28]. The staggered grid avoids these difficulties.

3.2.3. Stochastic fluxes. The stochastic flux $\boldsymbol{W}_c$, like other vectors, is represented on the faces of the grid; that is, $\boldsymbol{W}_c$ is a vector of independent and identically

distributed numbers, one number for each face of the grid. To calculate the state-dependent factor $\sqrt{c(1-c)}$ that appears in (29) on the faces of the grid, concentration is interpolated from the cell centers to the faces of the grid. At present, lacking any theoretical analysis, we use a simple arithmetic average (47) for this purpose.

The stochastic momentum flux $\boldsymbol{W_v}$ is represented on the faces of the shifted velocity grids, which for a uniform grid corresponds to the *cell centers* (i, j) and the *nodes* $(i + \frac{1}{2}, j + \frac{1}{2})$ of the grid [20]. Two random numbers need to be generated for each cell center, $W^{(x)}_{i,j}$ and $W^{(y)}_{i,j}$, corresponding to the diagonal of the stochastic stress tensor. Two additional random numbers need to be generated for each node of the grid, $W^{(x)}_{i+\frac{1}{2},j+\frac{1}{2}}$ and $W^{(y)}_{i+\frac{1}{2},j+\frac{1}{2}}$, corresponding to the off-diagonal components. In three dimensions, the three diagonal components of the stochastic stress are represented at the cell centers, while the six off-diagonal components are represented at the *edges* of the grid, two random numbers per edge, for example, $W^{(x)}_{i+\frac{1}{2},j+\frac{1}{2},k}$ and $W^{(y)}_{i+\frac{1}{2},j+\frac{1}{2},k}$.

For the incompressible equations, one can simply generate the different components of $\boldsymbol{W_v}$ as uncorrelated normal variates with mean zero and unit variance and obtain the correct equilibrium covariances. Alternatively, each realization of the stochastic stress can be made strictly symmetric and traceless as for compressible flow, as specified in (10). Because of the symmetry, in practice for each node or edge of the grid we generate only a single unit normal variate representing the two diagonally symmetric components. For each cell center, we represent the diagonal components by generating d independent normal random numbers of variance 2 and then subtracting their average from each number. Note that for collocated velocities a different approach is required because the diagonal and diagonally symmetric components of the stress tensor are not discretized on the same grid [28].

3.2.4. Advection. We now consider skew-adjoint discretizations of the advection operator $\boldsymbol{S} = \boldsymbol{DU}$ on a staggered grid. This problem has been considered in a more general context for the purpose of constructing stable methods for turbulent flow in [77, 78]; here we focus on a simple second-order centered discretization. The importance of the skew-adjoint condition in turbulent flow simulation is that it leads to strict discrete energy conservation for inviscid flow, which not only endows the schemes with long-time stability properties but also removes undesirable numerical dissipation. Conservation of the discrete kinetic energy $E_k = \rho\,(\boldsymbol{v}\cdot\boldsymbol{v})\,/2$ is also one of the crucial ingredients for fluctuation-dissipation balance, i.e., the requirement that the Gibbs–Boltzmann distribution $Z^{-1}\exp\left[-E_k/\left(k_BT\right)\right]$ be the invariant distribution of the stochastic velocity dynamics [19, 25, 79].

Consider first the spatial discretization of the advective term $\boldsymbol{DUc}$ in the concentration equation. Since divergence acts on vectors, which are represented on the faces of the grid, $\boldsymbol{Uc}$ should be represented on the faces as well; that is, $\boldsymbol{U}$ is a linear operator that maps from cell centers to faces and is a consistent discretization of the advective flux $c\boldsymbol{v}$. If we define an advection velocity $\boldsymbol{u}$ on the faces of the grid and also define a concentration on each face of the grid, then the advective flux can directly be calculated on each face. For example, for the x faces,

$$(c\boldsymbol{v})_x \to (\boldsymbol{Uc})^{(x)}_{i+\frac{1}{2},j} = u^{(x)}_{i+\frac{1}{2},j}\, c_{i+\frac{1}{2},j}. \tag{46}$$

For concentration, we can take $\boldsymbol{u} = \boldsymbol{v}$ since the velocity is already represented on the faces of the scalar grid. Simple averaging can be used to interpolate scalars from cells

to faces, for example,

$$c_{i+\frac{1}{2},j} = \frac{1}{2}\left(c_{i+1,j} + c_{i,j}\right), \tag{47}$$

although higher-order centered interpolations can also be used [28].

As discussed in section 3.2.1, we require that the advection operator be skew adjoint if $\boldsymbol{DU1} = \boldsymbol{Du} = \boldsymbol{0}$. Our temporal discretization of the incompressible equations (33)–(34) ensures that a discretely divergence-free velocity is used for advecting all variables. The case of compressible flow will be discussed further in section 3.2.5. In the incompressible case, $\boldsymbol{S} = \boldsymbol{DU}$ can be viewed as a second-order discretization of the "skew-symmetric" form of advection [77]

$$\boldsymbol{v}\cdot\boldsymbol{\nabla}c = \boldsymbol{v}\cdot\boldsymbol{\nabla}c + \frac{c}{2}\boldsymbol{\nabla}\cdot\boldsymbol{v} = \frac{1}{2}\left[\boldsymbol{\nabla}\cdot(c\boldsymbol{v}) + \boldsymbol{v}\cdot\boldsymbol{\nabla}c\right].$$

Namely, using (46) we obtain

$$(\boldsymbol{DUc})_{i,j} = \Delta x^{-1}\left(u^{(x)}_{i+\frac{1}{2},j}c_{i+\frac{1}{2},j} - u^{(x)}_{i-\frac{1}{2},j}c_{i-\frac{1}{2},j}\right) + \Delta y^{-1}\left(u^{(y)}_{i,j+\frac{1}{2}}c_{i,j+\frac{1}{2}} - u^{(y)}_{i,j-\frac{1}{2}}c_{i,j-\frac{1}{2}}\right)$$

and rewrite the x term using (47) as

$$\begin{aligned}&\left(u^{(x)}_{i+\frac{1}{2},j}c_{i+\frac{1}{2},j} - u^{(x)}_{i-\frac{1}{2},j}c_{i-\frac{1}{2},j}\right)\\ &\quad= \frac{1}{2}\left[\left(u^{(x)}_{i+\frac{1}{2},j}c_{i+1,j} - u^{(x)}_{i-\frac{1}{2},j}c_{i-1,j}\right) + c_{i,j}\left(u^{(x)}_{i+\frac{1}{2},j} - u^{(x)}_{i-\frac{1}{2},j}\right)\right],\end{aligned}$$

and similarly for the y term, to obtain

$$(\boldsymbol{DUc})_{i,j} = (\boldsymbol{Sc})_{i,j} = \left(\widetilde{\boldsymbol{S}}\boldsymbol{c}\right)_{i,j} + \frac{1}{2}c_{i,j}\left(\boldsymbol{Du}\right)_{i,j}, \tag{48}$$

where $\widetilde{\boldsymbol{S}}$ is a centered discretization of $\left[\boldsymbol{\nabla}\cdot(c\boldsymbol{v}) + \boldsymbol{v}\cdot\boldsymbol{\nabla}c\right]/2$:

$$\begin{aligned}\left(\widetilde{\boldsymbol{S}}\boldsymbol{c}\right)_{i,j} = \frac{1}{2}\Big[&\Delta x^{-1}\left(u^{(x)}_{i+\frac{1}{2},j}c_{i+1,j} - u^{(x)}_{i-\frac{1}{2},j}c_{i-1,j}\right)\\ &+ \Delta y^{-1}\left(u^{(y)}_{i,j+\frac{1}{2}}c_{i,j+1} - u^{(y)}_{i,j-\frac{1}{2}}c_{i,j-1}\right)\Big].\end{aligned} \tag{49}$$

Since the advection velocity is discretely divergence free, $\boldsymbol{S} = \widetilde{\boldsymbol{S}}$.

It is not hard to show that $\widetilde{\boldsymbol{S}}$ is skew-adjoint. Consider the x term in $\left[\widetilde{\boldsymbol{S}}\boldsymbol{c}\right]\cdot\boldsymbol{w}$, and, assuming periodic boundary conditions, shift the indexing from i to $i-1$ in the first sum and from i to $i+1$ in the second sum, to obtain

$$\sum_{i,j} w_{i,j}\left(u^{(x)}_{i+\frac{1}{2},j}c_{i+1,j} - u^{(x)}_{i-\frac{1}{2},j}c_{i-1,j}\right) = -\sum_{i,j} c_{i,j}\left(u^{(x)}_{i+\frac{1}{2},j}w_{i+1,j} - u^{(x)}_{i-\frac{1}{2},j}w_{i-1,j}\right).$$

Therefore, $\widetilde{\boldsymbol{S}}$ is skew-adjoint, $\left(\widetilde{\boldsymbol{S}}\boldsymbol{c}\right)\cdot\boldsymbol{w} = -\boldsymbol{c}\cdot\left(\widetilde{\boldsymbol{S}}\boldsymbol{w}\right)$. A similar transformation can be performed with slip or stick boundary conditions as well. These calculations show that (44) holds, and thus the discrete advection operator is skew-adjoint, as desired. Note that the additional terms in (15) due to the Soret effect can be included by advecting concentration with the effective velocity $\boldsymbol{u} = \boldsymbol{v} - \chi S_T\boldsymbol{\nabla}T$.

The same approach we outlined above for concentration can be used to advect the velocities as well. Each velocity component lives on its own staggered grid, and

advection velocities are needed on the faces of the shifted grid, which in two dimensions corresponds to the cell centers and the nodes of the grid. The velocity $\boldsymbol{v}_x$ is advected using an advection velocity field $\boldsymbol{u}^{(x)}$ that is obtained via a second-order interpolation of $\boldsymbol{v}$,

$$\left(u_x^{(x)}\right)_{i,j} = \frac{1}{2}\left(v^{(x)}_{i-\frac{1}{2},j} + v^{(x)}_{i+\frac{1}{2},j}\right),$$
$$\left(u_y^{(x)}\right)_{i+\frac{1}{2},j+\frac{1}{2}} = \frac{1}{2}\left(v^{(y)}_{i,j+\frac{1}{2}} + v^{(y)}_{i+1,j+\frac{1}{2}}\right),$$

and similarly for the other components. It is not hard to verify that the advection velocity $\boldsymbol{u}^{(x)}$ is discretely divergence-free if $\boldsymbol{v}$ is

$$\left(\boldsymbol{D}^{(x)}\boldsymbol{u}^{(x)}\right)_{i+\frac{1}{2},j} = \frac{1}{2}\left[(\boldsymbol{D}\boldsymbol{v})_{i,j} + (\boldsymbol{D}\boldsymbol{v})_{i+1,j}\right],$$

showing that $\boldsymbol{D}^{(x)}\boldsymbol{u}^{(x)} = \boldsymbol{0}$ if $\boldsymbol{D}\boldsymbol{v} = \boldsymbol{0}$. Therefore, the shifted advection operator $\boldsymbol{S}^{(x)} = \boldsymbol{D}^{(x)}\boldsymbol{U}^{(x)}$ is also skew-adjoint, as desired. Identical considerations apply for the other components of the velocity.

3.2.5. Compressible equations. It is instructive at this point to summarize our spatial discretization of the incompressible equations (14)–(15) before turning to the compressible equations. The concentration equation (15) is discretized as

$$\frac{d\boldsymbol{c}}{dt} = -\boldsymbol{D}\boldsymbol{U}\boldsymbol{c} + \chi\boldsymbol{D}\boldsymbol{G}\boldsymbol{c} + \boldsymbol{D}\boldsymbol{\Psi}, \tag{50}$$

where $\boldsymbol{U}$ is given by (46) with advection velocity $\boldsymbol{u} = \boldsymbol{v} - \chi S_T \boldsymbol{\nabla} T$. For the x component of the velocity, we use the spatial discretization

$$\frac{d\boldsymbol{v}_x}{dt} + (\boldsymbol{G}\boldsymbol{\pi})_x = -\boldsymbol{D}^{(x)}\boldsymbol{U}^{(x)}\boldsymbol{v}_x + \eta\boldsymbol{D}^{(x)}\boldsymbol{G}^{(x)}\boldsymbol{v}_x + \rho^{-1}\boldsymbol{D}^{(x)}\boldsymbol{\Sigma}^{(x)},$$

and similarly for the other components, and the pressure ensures that $\boldsymbol{D}\boldsymbol{v} = \boldsymbol{0}$.

Our staggered spatial discretization of the compressible equations (6)–(8) is closely based on the discretization described above for the incompressible equations. An important difference is that for compressible flow we use the conservative form of the equations; that is, we use the mass density ρ, the momentum density $\boldsymbol{j} = \rho\boldsymbol{v}$, and the partial mass density $\rho_1 = c\rho$ as variables. The momentum densities are staggered with respect to the mass densities. Staggered velocities are defined by interpolating density from the cell centers to the faces of the grid, for example,

$$\boldsymbol{v}^{(x)}_{i+\frac{1}{2},j} = \boldsymbol{j}^{(x)}_{i+\frac{1}{2},j}/\rho_{i+\frac{1}{2},j} = 2\boldsymbol{j}^{(x)}_{i+\frac{1}{2},j}/\left(\rho_{i+1,j} + \rho_{i,j}\right),$$

which implies that $\boldsymbol{D}\boldsymbol{j} = \boldsymbol{D}\boldsymbol{U}\boldsymbol{\rho}$.

The density equation (6) is discretized spatially as

$$\frac{d\boldsymbol{\rho}}{dt} = -\boldsymbol{D}\boldsymbol{U}\boldsymbol{\rho}, \tag{51}$$

while for the concentration equation (8) we use

$$\frac{d\boldsymbol{\rho}_1}{dt} = -\boldsymbol{D}\boldsymbol{U}\boldsymbol{\rho}_1 + \rho_0\chi_0\boldsymbol{D}\boldsymbol{G}\boldsymbol{c} + \boldsymbol{D}\boldsymbol{\Psi}, \tag{52}$$

where we assume that $\rho\chi = \rho_0\chi_0$ is constant. For the x component of the momentum density, we use

$$\frac{d\boldsymbol{j}_x}{dt} = -\boldsymbol{D}^{(x)}\boldsymbol{U}^{(x)}\boldsymbol{j}_x - c_T^2\left(\boldsymbol{G}\boldsymbol{\rho}\right)_x + \eta\boldsymbol{D}^{(x)}\boldsymbol{G}^{(x)}\boldsymbol{v}_x + \left(\zeta + \frac{\eta}{3}\right)\left(\boldsymbol{G}\boldsymbol{D}\boldsymbol{v}\right)_x + \boldsymbol{D}^{(x)}\boldsymbol{\Sigma}^{(x)}, \tag{53}$$

and similarly for the other components. The spatio-temporal discretization ensures strict local conservation of ρ, $\boldsymbol{j}$, and ρ_1.

The discretization (51)–(53) satisfies DFDB at equilibrium, specifically, the equilibrium covariances of velocity and density are $\langle \boldsymbol{v}\boldsymbol{v}^\star\rangle = \rho_0^{-1}k_BT_0\,\boldsymbol{I}$ and $\langle \boldsymbol{\rho}\boldsymbol{\rho}^\star\rangle = \rho_0 k_BT_0/c_T^2\,\boldsymbol{I}$, in agreement with the continuum spectra given in (17). Linearizing the semidiscrete density equation (51) around an equilibrium state $(\boldsymbol{\rho}, \boldsymbol{v}) = (\boldsymbol{\rho}_0 + \delta\boldsymbol{\rho},\, \boldsymbol{v}_0 + \delta\boldsymbol{v})$ with $\boldsymbol{D}\boldsymbol{v}_0 = \boldsymbol{0}$ gives

$$\frac{d\left(\delta\boldsymbol{\rho}\right)}{dt} + \widetilde{\boldsymbol{S}}_0\left(\delta\boldsymbol{\rho}\right) = -\rho_0\left[\boldsymbol{D}\left(\delta\boldsymbol{v}\right)\right].$$

Recall that the operator $\widetilde{\boldsymbol{S}}_0$, defined by (49) with $\boldsymbol{u} = \boldsymbol{v}_0$, is skew-adjoint, and the fluctuations in density are thus controlled by the coupling with the velocity fluctuations. For simplicity, consider this coupling for the case of a fluid at rest, $\boldsymbol{v}_0 = \boldsymbol{0}$, and thus $\delta\boldsymbol{j} = \rho_0\left(\delta\boldsymbol{v}\right)$. Linearizing the momentum update (53) and focusing on the coupling with the density fluctuations, we obtain

$$\frac{d\left(\delta\boldsymbol{v}\right)}{dt} + \text{advection} = -\rho_0^{-1}c_T^2\left[\boldsymbol{G}\left(\delta\boldsymbol{\rho}\right)\right] + \text{dissipation and forcing}.$$

Fluctuation-dissipation balance requires the skew-symmetry property $\boldsymbol{L}_{\rho,\boldsymbol{v}}\langle \boldsymbol{v}\boldsymbol{v}^\star\rangle = -\langle \boldsymbol{\rho}\boldsymbol{\rho}^\star\rangle\,\boldsymbol{L}_{\boldsymbol{v},\rho}^\star$, where $\boldsymbol{L}_{\rho,\boldsymbol{v}} = -\rho_0\boldsymbol{D}$ is the operator in front of $\delta\boldsymbol{v}$ in the density equation, and $\boldsymbol{L}_{\boldsymbol{v},\rho} = -c_T^2\boldsymbol{G}$ is the operator in front of $\delta\boldsymbol{\rho}$ in the velocity equation. This skew-symmetry requirement is satisfied because of the key duality property $\boldsymbol{D} = -\boldsymbol{G}^\star$. This demonstrates the importance of the duality between the discrete divergence and gradient operators, not just for a single advection-diffusion equation but also for coupling between the different fluid variables. In future work, we will explore generalizations of the concept of skew-adjoint discrete advection to the nonlinear compressible equations [56, 78].

3.2.6. Boundary conditions. Nonperiodic boundary conditions, specifically, Neumann or Dirichlet physical boundaries, can be incorporated into the spatial discretization by modifying the discrete divergence, gradient, and Laplacian operators near a boundary. This needs to be done in a way that not only produces an accurate and robust deterministic scheme but also ensures fluctuation-dissipation balance even in the presence of boundaries. Here we extend the approach first suggested in an appendix in [13] to the staggered grid. It can be shown that the inclusion of the (discrete) incompressibility constraint does not affect the fluctuation-dissipation balance when an unsplit Stokes solver is employed in the temporal integrator [46].

We assume that the physical boundary is comprised of faces of the grid. Since only the direction perpendicular to the wall is affected, we focus on a one-dimensional system in which there is a physical boundary between cells 1 and 0. For the component of velocity perpendicular to the wall, some of the grid points are on the physical boundary itself, and those values are held fixed and not included as independent degrees of freedom. For the second-order spatial discretization that we employ, no values in cells outside of the physical domain are required. Therefore, no special handling at the boundary is needed.

For cell-centered quantities, such as concentration and components of the velocity parallel to the wall, the boundary is half a cell away from the cell center; that is, the boundary is staggered. In this case we use the same discrete operators near the boundaries as in the interior of the domain, using *ghost cells* extending beyond the boundaries to implement the finite-difference stencils near the boundaries. One can think of this as a modification of the stencil of the Laplacian operator $\boldsymbol{L}$ near boundaries; specifically, when boundaries are present, the dissipative operator $\boldsymbol{L} \neq \boldsymbol{DG}$ but rather $\boldsymbol{L} = \boldsymbol{D}\widetilde{\boldsymbol{G}}$, where $\widetilde{\boldsymbol{G}}$ is a modified gradient. Repeating the calculation in (41) for the spatially discretized model equation

$$\frac{d\boldsymbol{c}}{dt} = \chi \boldsymbol{L}\boldsymbol{c} + \sqrt{2\chi/\left(\Delta V\, \Delta t\right)}\boldsymbol{D}\boldsymbol{W}$$

leads to a generalization of the DFDB condition (42), assuming $\boldsymbol{L}^\star = \boldsymbol{L}$:

$$\chi \boldsymbol{L}\boldsymbol{C}_{\boldsymbol{c}} + \chi \boldsymbol{C}_{\boldsymbol{c}}\boldsymbol{L}^\star = 2\chi \Delta V^{-1}\boldsymbol{L} = -2\chi \Delta V^{-1}\boldsymbol{D}\boldsymbol{C}_{\boldsymbol{W}}\boldsymbol{D}^\star \quad \Rightarrow \quad \boldsymbol{L} = -\boldsymbol{D}\boldsymbol{C}_{\boldsymbol{W}}\boldsymbol{D}^\star. \tag{54}$$

Consider first a Neumann condition on concentration, $\partial c(0)/\partial x = 0$. This means that a no-flux condition is imposed on the boundary, and therefore for consistency with physical conservation the stochastic flux on the boundary should also be set to zero, $W_{\frac{1}{2}} = 0$. The ghost cell value is set equal to the value in the neighboring interior cell (reflection), $c_0 = c_1$, leading to

$$(\boldsymbol{D}\boldsymbol{W})_1 = \Delta x^{-1} W_{\frac{3}{2}}, \quad \left(\widetilde{\boldsymbol{G}}\boldsymbol{c}\right)_{\frac{1}{2}} = 0, \quad (\boldsymbol{L}\boldsymbol{c})_1 = \Delta x^{-2}\left(c_2 - c_1\right). \tag{55}$$

If we exclude points on the boundary from the domain of the divergence operator, which is also the range (image) of the gradient operator, then it is not hard to see that the duality condition $\boldsymbol{D}^\star = -\widetilde{\boldsymbol{G}}$ continues to hold. We can therefore continue to use uncorrelated unit normal variates for the stochastic fluxes not on the boundary, $\boldsymbol{C}_{\boldsymbol{W}} = \boldsymbol{I}$ in (54).

If a Dirichlet condition $c(0) = 0$ is imposed, then the ghost cell value is obtained by a linear extrapolation of the value in the neighboring interior cell (inverse reflection), $c_0 = -c_1$, leading to

$$(\boldsymbol{D}\boldsymbol{W})_1 = \Delta x^{-1}\left(W_{\frac{3}{2}} - W_{\frac{1}{2}}\right), \quad \left(\widetilde{\boldsymbol{G}}\boldsymbol{c}\right)_{\frac{1}{2}} = \Delta x^{-1}\left(2c_1\right), \quad (\boldsymbol{L}\boldsymbol{c})_1 = \Delta x^{-2}\left(c_2 - 3c_1\right). \tag{56}$$

The duality condition is no longer satisfied, $\boldsymbol{D}^\star \neq -\widetilde{\boldsymbol{G}}$, but it is not hard to show that the fluctuation-dissipation balance condition (54) can be satisfied by simply doubling the variance of the stochastic flux on the boundary, $\langle W_{\frac{1}{2}} W_{\frac{1}{2}}^\star \rangle = 2$. Note that the Laplacian (56) is not formally second-order accurate at the boundary; however, its normal modes (eigenvectors) can be shown to correspond exactly to the normal modes of the continuum Laplacian and have decay rates (eigenmodes) that are second-order accurate in Δx^2, and in practice, pointwise second-order accuracy is observed even next to the boundary. Formal second-order local accuracy can be obtained by using a quadratic extrapolation for the ghost cell, $c_0 = -2c_1 + c_2/3$ and $(\boldsymbol{L}\boldsymbol{c})_1 = \Delta x^{-2}\left(4c_2/3 - 4c_1\right)$; however, this requires a more complicated handling of the stochastic fluxes near the boundary as well.

In summary, the only change required to accommodate physical boundaries is to set the variance of stochastic fluxes on a physical boundary to zero (at Neumann

boundaries) or to twice that used for the interior faces (at Dirichlet boundaries). For density in compressible flows, the ghost cell values are generated so that the pressure in the ghost cells is equal to the pressure in the neighboring interior cell, which ensures that there is no unphysical pressure gradient in the momentum equation across the interface. There is also no stochastic mass flux through faces on the boundary independent of the type of boundary condition at the wall. For incompressible flow, the gradient of pressure is discretized as $\boldsymbol{G}\pi = -\boldsymbol{D}^\star\pi$ even in the presence of stick or slip boundary conditions for velocity; more complicated velocity-stress or open [27] boundary conditions are simple to handle with the projection-preconditioner solvers, at least in the deterministic setting.

4. Implementation and numerical tests. We now describe in more detail our implementations of the spatio-temporal discretizations described in section 3 and provide numerical evidence of their ability to reproduce the correct fluctuation spectrum in uniform flows with periodic boundary conditions. A less trivial application with nonperiodic boundaries is studied in section 5.

We consider here a uniform periodic system in which there is a steady background (mean) flow of velocity $\boldsymbol{v}_0$. Unlike the continuum formulation, the discrete formulation is not Galilean-invariant under such uniform motion and the covariance of the discrete fluctuations is affected by the magnitude of $\boldsymbol{v}_0$. The stability and accuracy of the spatio-temporal discretization is controlled by the dimensionless CFL numbers

$$\alpha = \frac{V\Delta t}{\Delta x}, \quad \beta = \frac{\nu\Delta t}{\Delta x^2}, \quad \beta_c = \frac{\chi\Delta t}{\Delta x^2},$$

where $V = c_T$ (isothermal speed of sound) for low Mach number compressible flow, $V = \|\boldsymbol{v}_0\|_\infty$ for incompressible flow, and typically $\chi \ll \nu$. The explicit handling of the advective terms places a stability condition $\alpha \lesssim 1$, and the explicit handling of diffusion in the compressible flow case requires $\max(\beta, \beta_c) \leq 1/(2d)$, where d is the dimensionality. The strength of advection relative to dissipation is measured by the cell Reynolds number $r = \alpha/\beta = V\Delta x/\nu$.

To characterize the weak accuracy of our methods we examine the discrete Fourier spectra of the fluctuating fields at equilibrium and compare them to the continuum theory discussed in section 2.2 for all discrete wavenumbers $\boldsymbol{k}$. We use subscripts to denote which pair of variables is considered, and normalize each covariance so that for self-correlations we report the relative error in the variance, and for cross-correlations we report the correlation coefficient between the two variables. For example, the nondimensionalized static structure factor for concentration is

$$\tilde{S}_{c,c} = \frac{\langle \hat{c}\hat{c}^\star \rangle}{\Delta V^{-1} S_{c,c}} = \frac{\Delta V}{M\rho_0^{-1}\, c_0(1-c_0)} \langle \hat{c}\hat{c}^\star \rangle \,,$$

where $\hat{c}(\boldsymbol{k})$ is the discrete Fourier transform of the concentration. Note that an additional factor equal to the total number of cells may be needed in the numerator depending on the exact definition used for the discrete Fourier transform [28]. Similarly, the cross-correlations between different variables need to be examined as well, such as, for example,

$$\tilde{\boldsymbol{S}}_{c,\boldsymbol{v}} = \frac{\Delta V}{\sqrt{\left[M\rho_0^{-1}\, c_0(1-c_0)\right]\left(\rho_0^{-1} k_B T_0\right)}} \langle \hat{c}\hat{\boldsymbol{v}}^\star \rangle \,.$$

For staggered variables, the shift between the corresponding grids should be taken into account as a phase shift in Fourier space, for example, $\exp(k_x\Delta x/2)$ for v_x.

For a perfect scheme, $\tilde{S}_{c,c} = 1$ and $\tilde{\boldsymbol{S}}_{c,\boldsymbol{v}} = \boldsymbol{0}$ for all wavenumbers, and DFDB in our discretization ensures this in the limit $\Delta t \to 0$. Our goal will be to quantify the deviations from "perfect" for several methods as a function of the dimensionless numbers α and β.

4.1. Incompressible solver. We have implemented the incompressible scheme described in sections 3.1.2 and 3.2 using the IBAMR software framework [80], an open-source library for developing fluid-structure interaction models that use the immersed boundary method. The IBAMR framework uses SAMRAI [81] to manage Cartesian grids in parallel, and it uses PETSc [82] to provide iterative Krylov solvers. The majority of the computational effort in the incompressible solver is spent in the linear solver for the Stokes system; in particular, it is spent in the projection-based preconditioner, the application of which requires solving a linear Poisson system for the pressure and a modified linear Helmholtz system for the velocities and the concentrations [34]. For small viscous CFL numbers $\beta \ll 1$, the Poisson solver dominates the cost; however, for $\beta \gg 1$, the Helmholtz linear systems become similarly ill-conditioned and require a good preconditioner themselves. We employ the *hypre* library [83] to solve the linear systems efficiently using geometric multigrid solvers.

For incompressible flow, one could directly compare the spectrum of the velocities $\langle \hat{\boldsymbol{v}} \hat{\boldsymbol{v}}^\star \rangle$ to the spectrum of the discrete projection operator $\mathbb{P}$ (see section 3.2.1). It is, however, simpler and more general to instead examine the equilibrium covariance of the discrete modes forming an orthonormal basis for the space of discretely divergence-free modes. The amplitude of all modes should be unity, even if there are physical boundaries present, making it easy to judge the accuracy at different wavenumbers. For periodic boundary conditions, a discretely orthogonal basis is obtained by replacing the wavenumber $\boldsymbol{k} = (k_x, k_y, k_z)$ in (23)–(25) by the effective wavenumber $\tilde{\boldsymbol{k}}$ that takes into account the centered discretization of the projection operator, for example,

$$\tilde{k}_x = \frac{\exp(ik_x\Delta x/2) - \exp(-ik_x\Delta x/2)}{i\Delta x} = k_x \frac{\sin(k_x\Delta x/2)}{(k_x\Delta x/2)}. \tag{57}$$

Our temporal discretization ensures that the discrete velocities are discretely divergence-free; that is, $\langle \hat{v}_1 \hat{v}_1^\star \rangle = 0$ to within the tolerance of the linear solvers used for the Stokes system. For a perfect scheme, the dimensionless structure factor

$$\tilde{S}_{\boldsymbol{v}}^{(2)} = \frac{\Delta V}{\rho_0^{-1} k_B T_0} \langle \hat{v}_2 \hat{v}_2^\star \rangle ,$$

and analogously $\tilde{S}_{\boldsymbol{v}}^{(3)}$ (in three dimensions), would be unity for all wavenumbers, while $\tilde{S}_{\boldsymbol{v}}^{(2,3)} \sim \langle \hat{v}_2 \hat{v}_3^\star \rangle$ would be zero.

Note that for a system at equilibrium, $\boldsymbol{\nabla} \bar{c} = \boldsymbol{0}$, the linearized velocity equation and the concentration equation (18) are uncoupled, and thus $\tilde{\boldsymbol{S}}_{c,\boldsymbol{v}} = \boldsymbol{0}$. Observe that the same temporal discretization is used for the velocity equation, projected onto the space of discretely divergence-free vector fields consistent with the boundary conditions, and for the concentration equation. Therefore, it is sufficient to present here numerical results for only one of the self-correlations $\tilde{S}_{\boldsymbol{v}}^{(2)}$, $\tilde{S}_{\boldsymbol{v}}^{(3)}$, or $\tilde{S}_{c,c}$. In Figure 2 we show $\tilde{S}_{\boldsymbol{v}}^{(2)}$ as a function of the wavenumber $\boldsymbol{k}$ in three dimensions for a cell Reynolds number $r = 1$ and advective CFL numbers $\alpha = 0.5$ and $\alpha = 0.25$. Even for the relatively large time step, the deviation from unity is less than 5%, and as $\alpha \to 0$ it can be shown theoretically and observed numerically that the correct covariance is obtained at all wavenumbers.

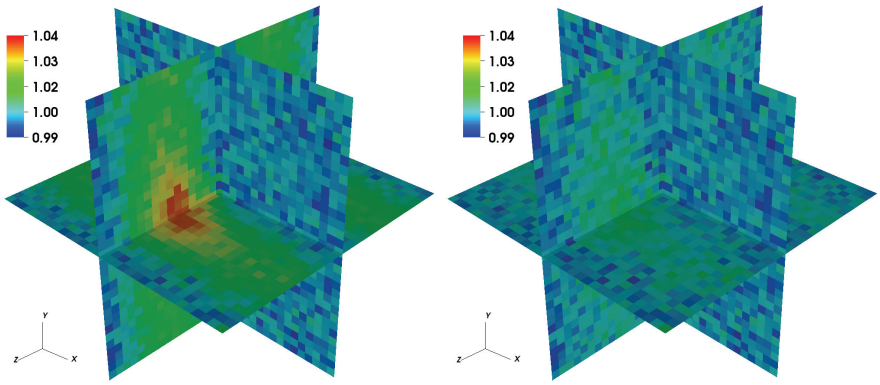

FIG. 2. *Spectral power of the first solenoidal mode for an incompressible fluid,* $\tilde{S}^{(2)}_{\boldsymbol{v}}(k_x, k_y, k_z)$, *as a function of the wavenumber (ranging from* 0 *to* $\pi/\Delta x$ *along each axis), for a periodic system with* 32^3 *cells. A uniform background flow along the* z *axis is imposed. The left panel is for a time step* $\alpha = 0.5$ *and the right for* $\alpha = 0.25$. *Though not shown, we find that* $\tilde{S}^{(3)}_{\boldsymbol{v}}$ *and* $\tilde{S}_{c,c}$ *are essentially identical, and both the real and imaginary parts of the cross-correlation* $\tilde{S}^{(2,3)}_{\boldsymbol{v}}$ *vanish to within statistical accuracy.*

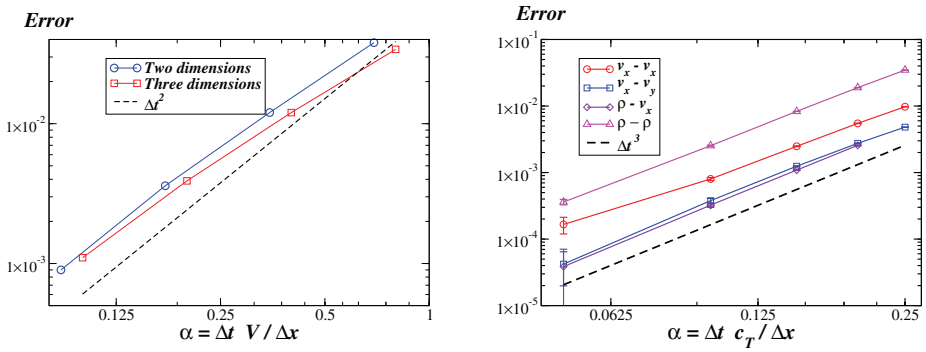

FIG. 3. *(Left) Relative error in the equilibrium variance of velocity (or, equivalently, concentration) for several time steps, as obtained using our incompressible code with a background flow velocity* $\boldsymbol{v}_0 = (\sqrt{3}, 2)/2$ *corresponding to cell Reynolds number* $r = \sqrt{3}/2$ *in two dimensions and* $\boldsymbol{v}_0 = (1, 1/3, 1/3)$ *corresponding to* $r = 1$ *in three dimensions, for a grid of size* 32^2 *and* 32^3 *cells, respectively. The theoretical order of convergence* $O(\Delta t^2)$ *is shown for comparison. Error bars are on the order of the symbol size. (Right) Normalized covariance of the discrete velocities and densities compared to the theoretical expectations, using the parameters reported in the caption of Figure* 4. *The value reported is the relative error of the variance of a variable or the correlation coefficient between pairs of variables; see the legend. The theoretical order of convergence* $O(\Delta t^3)$ *is shown for comparison. Error bars are indicated but are smaller than the symbol size except for the smallest time step.*

Theoretical analysis suggests that the error in the discrete covariance vanishes with the time step and the background velocity as $O(\alpha^2) \sim O\left(V^2 \Delta t^2\right)$ for both velocity and concentration [46]. In the left panel of Figure 3 we show the observed relative error in the variance of the discrete velocity as a function of α, confirming the predicted quadratic convergence. As expected, identical results are obtained for concentration as well. These numerical results confirm that our spatial discretization satisfies the DFDB condition and the temporal discretization is weakly second-order accurate.

4.2. Compressible solver. Unlike the incompressible method, which requires complex linear solvers and preconditioners, the explicit compressible scheme is very simple and easy to parallelize on graphics processing units (GPUs). Our implementation is written in the CUDA programming environment and is three-dimensional with the special case of $N_z = 1$ cell along the z axes corresponding to a quasi–two-dimensional system. In our implementation we create one thread per cell, and each thread writes only to the memory address associated with its cell and accesses only the memory associated with its own and neighboring cells. This avoids concurrent writes and costly synchronizations between threads, facilitating efficient execution on the GPU. Further efficiency is gained by using the GPU texture unit to perform some of the simple computations, such as evaluating the equation of state. Our GPU code running in a NVIDIA GeForce GTX 480 is about 4 times faster (using double precision) than a compressible CPU-based code [28] running on 32 AMD cores using MPI. Note that with periodic boundary conditions the velocity and the pressure linear systems in the incompressible formulation decouple, and fast Fourier transforms could be used to solve them efficiently. We have used this to also implement the incompressible algorithm on a GPU by using the NVIDIA FFT library as a Poisson/Helmholtz solver. We emphasize, however, that this approach is applicable only to the case of periodic boundary conditions.

We first examine the equilibrium discrete Fourier spectra of the density and velocity fluctuations for a uniform periodic system with an imposed background flow, with similar results observed for concentration fluctuations. In Figure 4 we show the correlations of density and velocity fluctuations as a function of the wavenumber $\boldsymbol{k}$ in three dimensions for a CFL number of $\alpha = 0.25$. We see that self-correlations are close to unity, while cross-correlations nearly vanish, as required, with density fluctuations having the largest relative error of 5% for the largest wavenumbers.

Calculating cross-correlations in real space is complicated by the staggering of the different grids. We arbitrarily associate the "upward" cell faces with the cell center, defining $\langle (\delta\rho)\,(\delta v_x)\rangle \equiv \langle (\delta\rho_{i,j})\,\big(\delta v^{(x)}_{i+\frac{1}{2},j}\big)\rangle$ and $\langle (\delta v_x)\,(\delta v_y)\rangle \equiv \langle \big(\delta v^{(x)}_{i+\frac{1}{2},j}\big)\big(\delta v^{(y)}_{i,j+\frac{1}{2}}\big)\rangle$. Theoretical analysis suggests that the error in the discrete covariance vanishes with the time step as $O(\alpha^3) \sim O\left(c_T^3 \Delta t^3\right)$ [46]. In the right panel of Figure 3 we show the relative error in the discrete covariances as a function of α in the presence of a background flow, confirming the predicted cubic convergence. These numerical results verify that our spatial discretization satisfies the DFDB condition and the temporal discretization is weakly third-order accurate.

4.2.1. Dynamic correlations. For compressible flow, the dynamics of the fluctuations is affected by the presence of sound waves, and it is important to verify that the numerical scheme is able to reproduce the temporal correlations between the fluctuations of the different pairs of variables. In particular, a good method should reproduce the dynamic correlations at small wavenumbers and wavefrequencies correctly [28]. Theoretical predictions for the equilibrium covariances of the spatio-temporal spectra of the fluctuating fields, usually referred to as *dynamic structure factors*, are easily obtained by solving the equations (6)–(7) in the Fourier wavevector-frequency $(\boldsymbol{k}, \omega)$ domain and averaging over the fluctuations of the stochastic forcing [17]. The density-density dynamic structure factor $S_{\rho,\rho}(\boldsymbol{k}, \omega)$ is accessible experimentally via light scattering measurements, and for isothermal flow it exhibits two symmetric Brilloin peaks at $\omega \approx \pm c_T k$. The velocity components exhibit an additional central Rayleigh peak at $\omega = 0$ due to the viscous dissipation. As the fluid becomes less compressible (i.e., the speed of sound increases), there is an increasing

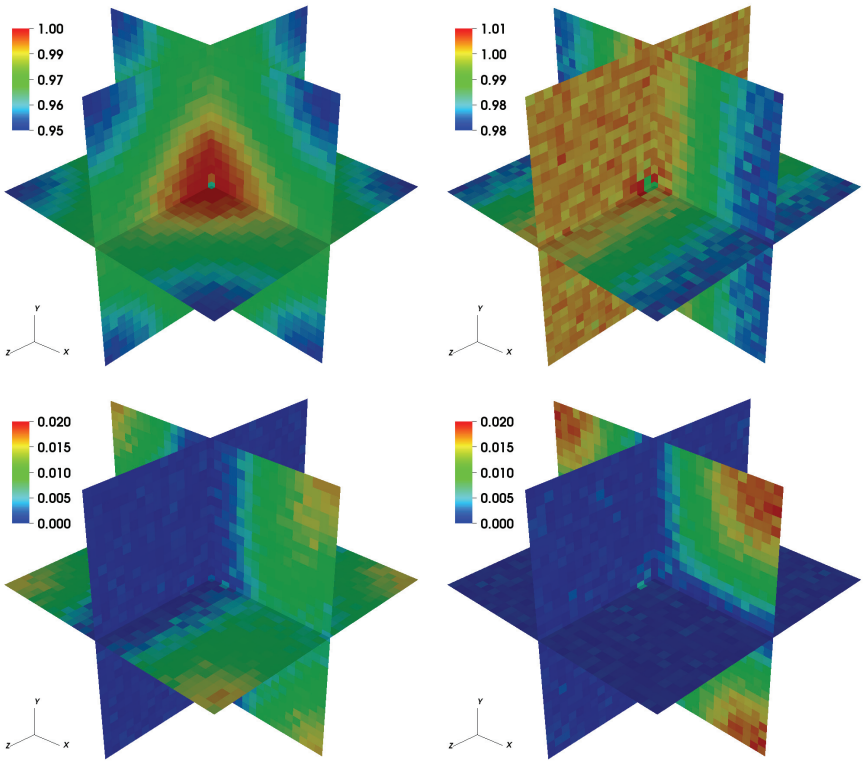

FIG. 4. *Normalized static structure factors* $\tilde{S}_{\rho,\rho}$ *(top left),* $\tilde{S}_{v_x,v_x}$ *(top right),* $\tilde{S}_{\rho,v_x}$ *(bottom left), and* $\tilde{S}_{v_x,v_y}$ *(bottom right) for a compressible fluid with physical properties similar to water for a periodic system with* 30^3 *cells. A uniform background flow with velocity* $v_0 = (0.2, 0.1, 0.05)c_T$ *is imposed, and the time step corresponds to an acoustic CFL number* $\alpha = 0.25$ *and viscous CFL number* $\beta_\nu = 0.017$ *for shear viscosity and* $\beta_\zeta = 0.041$ *for bulk viscosity.*

separation of time scales between the side and central spectral peaks, showing the familiar numerical stiffness of the compressible NS equations.

In Figure 5 we compare the theoretical to the numerical dynamic structure factors for one of the smallest resolved wavenumbers and observe very good agreement. Note that unlike static correlations, dynamic correlations are subject to discretization artifacts for larger wavenumbers, even as $\Delta t \to 0$ [28]. Specifically, the positions and widths of the various peaks are set by the effective wavevector $\tilde{\boldsymbol{k}}$ rather than the true wavevector $\boldsymbol{k}$, as given for the standard second-order discretization of diffusion in (57).

5. Giant fluctuations. As a nontrivial application of our staggered schemes for fluctuating hydrodynamics, we perform the first incompressible computer simulations of diffusive mixing in microgravity, recently studied experimentally aboard a satellite in orbit around the Earth [12]. The experimental data presented in [12] shows good agreement with theoretical predictions; however, various oversimplifications are made in the theory, and, notably, only the solenoidal velocity mode with the largest wavelength is considered. Numerical simulations allow for a more detailed comparison of experimental data with fluctuating hydrodynamics, at least within the applicability

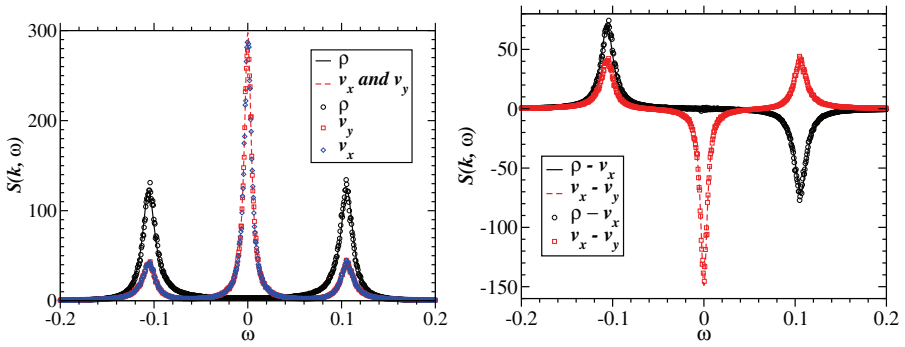

FIG. 5. *Numerical data (symbols) and theory (lines) for the real part of several dynamic structure factors for wavenumber* $\boldsymbol{k} = (2,2,2) \cdot 2\pi/L$ *in a cubic periodic box with* 30^3 *cells and volume* L^3. *Self-correlations are shown in the left panel, and cross-correlations are shown in the right panel. The imaginary part vanishes to within statistical accuracy for the off-diagonal terms. The physical parameters are as reported in the caption of Figure* 4.

of the physical approximations discussed in section 1.1.

The experimental configuration consists of a dilute solution of polystyrene in toluene, confined between two parallel transparent plates that are a distance $h = 1$mm apart. A steady temperature gradient $\nabla T = \Delta T/h$ is imposed along the y axes via the plates. The weak temperature gradient leads to a strong concentration gradient $\boldsymbol{\nabla}\bar{c} = \bar{c}S_T\boldsymbol{\nabla}T$ due to the Soret effect, giving rise to an exponential steady-state concentration profile $\bar{c}(y)$. Quantitative shadowgraphy is used to observe and measure the strength of the fluctuations in the concentration around $\bar{c}$ via the change in the refraction index. The observed light intensity, once corrected for the optical transfer function of the equipment, is proportional to the intensity of the fluctuations in the concentration averaged along the gradient:

$$c_\perp(x,z) = h^{-1}\int_{y=0}^{h} c(x,y,z)dy.$$

The main physical parameters we employed in our simulations are summarized in Table 1. Additional details of the experimental setup and parameters are given in [12].

The large speed of sound in toluene makes the compressible equations very stiff at the length scales of the experimental system. It is usually argued that compressibility does not affect the concentration fluctuations [17]. Solving the compressible equations in the presence of a concentration gradient confirms that, as long as there is a large separation of time scales between the acoustic and diffusive dynamics, the presence of sound waves does not affect the concentration fluctuations. In our compressible simulations, we artificially decrease the speed of sound many-fold and set the cell Reynolds number to $r = c_T\Delta x/\nu \geq 10$. Numerical results show that this is sufficient for approaching the limit $r \to \infty$ to within the statistical accuracy of our results. This decrease in c_T corresponds to making the mass of the toluene molecules much larger than the mass of the polystyrene macromolecules themselves, which is of course physically very unrealistic. One can think of our compressible simulations of giant fluctuations in microgravity as an artificial compressibility method for solving the incompressible equations.

In the actual experiments reported in [12], concentration diffusion is much slower than momentum diffusion, corresponding to Schmidt number $S_c = \nu/\chi \approx 3\cdot 10^3$. This

TABLE 1
Summary of parameters used in the simulations of giant fluctuations in zero gravity.

Parameter	Value	Notes
ρ	0.86 gr/cm^3	on average only if compressible
$\chi(\nu+\chi)$	$1.2 \cdot 10^{-8}$ cm^4/s^2	kept constant in all runs
ν	variable $S_c = \nu/\chi$	physical value $\nu = 6.07 \cdot 10^{-3}$ cm^2/s
χ	variable $S_c = \nu/\chi$	physical value $\chi = 1.97 \cdot 10^{-6}$ cm^2/s
ζ	0	none for incompressible
$k_B T$	$4.18 \cdot 10^{-14}$ gr cm^2/s	corresponds to $T = 303$ K
M	$1.51 \cdot 10^{-20}$ gr	not important for results
S_T	0.0649 K^{-1}	enters only via $S_T \boldsymbol{\nabla} T$
c_0	0.018	on average only if nonperiodic
c_T	1.11 cm/s	physical value $c_T \approx 1.3 \cdot 10^5$ cm/s

level of stiffness makes direct simulation of the temporal dynamics of the fluctuations infeasible, as long averaging is needed to obtain accurate steady-state spectra, especially for small wavenumbers. However, as far as the nonequilibrium static correlations are concerned, we see from (27) that the crucial quantity is $\chi(\nu+\chi) = (s+1)\chi^2$, rather than χ and ν individually. Therefore, we can artificially increase χ and decrease ν to reduce s, keeping $s \gg 1$ and $(s+1)\chi^2$ fixed. In the linearized case, it can be proven more formally that there exists a limiting stochastic process for the concentration as $s \to \infty$ so long as $s\chi^2$ is kept constant [84]. In fact, artificially decreasing the Schmidt number while keeping $s\chi^2$ fixed can be seen as an instance of the *seamless* multiscale method presented in [85].

5.1. Approximate theory. For large wavenumbers, the influence of the boundaries can be neglected and the periodic theory presented in section 2.2.1 applied. In order to demonstrate the importance of the boundaries, and also to test the code by comparing to the periodic theory, we have implemented a model in which qualitatively similar giant concentration fluctuations appear even though the macroscopic concentration profile is uniform, $\bar{c}(y) = c_0$. Numerically, this sort of quasi-periodic model is implemented by using periodic boundary conditions but adding an additional source term $-\boldsymbol{v} \cdot \boldsymbol{\nabla} \bar{c}$ in the concentration equation, as in (18). This term mimics our skew-adjoint discretization of the advection by the fluctuating velocities

$$\boldsymbol{v} \cdot \boldsymbol{\nabla} \bar{c} \to (\boldsymbol{D}\boldsymbol{U}\bar{\boldsymbol{c}})_{i,j} = \frac{\nabla \bar{c}}{2} \left(v^{(y)}_{i,j+\frac{1}{2}} + v^{(y)}_{i,j-\frac{1}{2}} \right)$$

and is conservative when integrated over the whole domain. Note that in this quasi-periodic setup $\boldsymbol{\nabla} \bar{c}$ is simply an externally imposed quantity unrelated to the actual mean concentration profile. We emphasize that these quasi-periodic simulations are used only for testing and theoretical analysis of the problem, and not for comparison with the experimental results. In the simulations with physical boundaries and in the experiments the concentration profile is exponential rather than linear. For the purposes of constructing a quasi-periodic approximation, we take the effective concentration gradient to be $\nabla \bar{c} \approx \Delta c/h$, where Δc is the difference in concentration near the two boundaries.

For periodic systems, the spectrum of the fluctuations of $c_\perp$ can be obtained from the full three-dimensional spectrum (27) by setting $k_y = k_\parallel = 0$. For the specific parameters in question, the equilibrium fluctuations in concentration are negligible

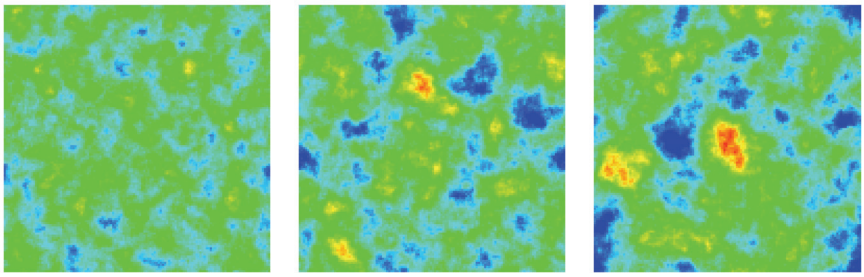

FIG. 6. *Snapshots of the concentration $c_\perp$ in the plane perpendicular to the gradient $\boldsymbol{\nabla}\bar{c}$ at times $0.1\tau_0$, τ_0, and $5\tau_0$ after the gradient is established. The thickness of the sample (perpendicular to the page) is one quarter of the lateral extents of the system, $h = L_y = L_x/4$, and sets the scale of the steady-state fluctuations. Compare to the experimental snapshots shown in Figure 1 of* [12].

even at the largest resolved wavenumbers. When discretization artifacts are taken into account, the quasi-periodic theoretical prediction for the experimentally observed spectrum becomes

$$S^{\perp}_{\mathrm{QP}}(k_x,k_z) = \left\langle \left(\widehat{\delta c}_\perp\right)\left(\widehat{\delta c}_\perp\right)^{\star}\right\rangle = \frac{k_B T}{\rho\left[\chi(\nu+\chi)\right]\tilde{k}_\perp^4}\left(\nabla\bar{c}\right)^2, \tag{58}$$

where $\tilde{k}_\perp^4 = \left(\tilde{k}_x^2+\tilde{k}_z^2\right)^2$ and the tilde denotes the effective wavenumber (57). Imposing no-slip conditions for the fluctuating velocities makes the theory substantially more complicated. A single-mode approximation for the velocities is made in [62] in order to obtain a closed-form expression for the spectrum of concentration fluctuations in a nonperiodic system $S^{\perp}_{\mathrm{NP}}$. For a small Lewis number and without gravity, it is found that

$$\frac{S^{\perp}_{\mathrm{NP}}(\boldsymbol{k}_\perp)}{S^{\perp}_{\mathrm{QP}}(\boldsymbol{k}_\perp)} \approx G(hk_\perp) = \frac{q_\perp^4}{q_\perp^4 + 24.6q_\perp^2 + 500.5}, \tag{59}$$

where $q_\perp = hk_\perp$ is a nondimensionalized wavenumber.

The Galerkin function G given by (59) reflects the physical intuition that the no-slip condition suppresses fluctuations at scales larger than the distance between the physical boundaries [12]. After the concentration gradient is established, "giant" [42] concentration fluctuations evolve with a typical time scale of $\tau_0 = h^2/(\pi^2\chi) \sim 1000$s, until a steady state is reached in which the typical length scale of the concentration fluctuations is set by the finite extent of the domain. This is illustrated in Figure 6 via snapshots of $c_\perp(x,z;\,t)$ taken at several points in time after starting with no concentration fluctuations at time $t = 0$.

5.2. Simulations and results. In our simulations, the plates are represented by no-slip boundaries at $y = 0$ and $y = h$, and periodic boundaries are imposed along the x and z axes to mimic the large extents of the system in the directions perpendicular to the gradient. A Robin boundary condition is used for concentration at the physical boundary,

$$\frac{\partial c}{\partial n} = -c\left(\boldsymbol{n}\cdot\boldsymbol{v}_s\right),$$

ensuring that the normal component of the concentration flux vanishes at a physical boundary. The stochastic concentration flux also vanishes at the boundary as for

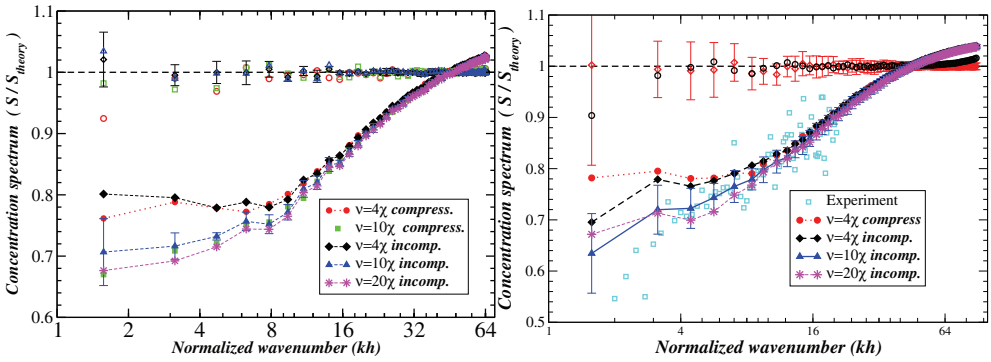

FIG. 7. *Ratio between the numerical and theoretical discrete spectra of concentration projected along the y axes as a function of the normalized wavenumber* $q_\perp = k_\perp h$. *For all runs* $N_y = 32$ *cubic hydrodynamic cells along the y axes were used, and all systems have aspect ratio* $N_x/N_y = N_z/N_y = 4$. *Error bars are indicated for some of the curves to indicate the typical level of statistical uncertainty. (Left) Two dimensions, for both compressible and incompressible fluids (see the legend), with either periodic boundary conditions (empty symbols) or physical boundaries (solid symbols) imposed at the y boundaries for several Schmidt numbers* $S_c = \nu/\chi$. *(Right) Three dimensions, with the same symbols as the left panel), along with arbitrarily normalized experimental data* [12] *(see the legend) corresponding to* $S_c \approx 3 \cdot 10^3$ *(experimental measurements courtesy of A. Vailati).*

Dirichlet boundaries since the Soret term does not affect fluctuation-dissipation balance. In the codes the boundary condition is imposed by setting the concentration in a ghost cell to

$$c_g = c_n \frac{2 \pm v_s \Delta y}{2 \mp v_s \Delta y},$$

where c_n is the value in the neighboring cell in the interior of the computational domain, and the sign depends on whether the ghost cell is at the low or high end of the y axis. The boundary condition is imposed explicitly, which leads to nonconservation of the total concentration when a semi-implicit method is used for the diffusive terms in the concentration equation. This can be corrected by implementing the boundary condition implicitly or using an explicit method for concentration; however, we do not do either since the observed change in the average concentration is small for the specific parameters we use.

Using the incompressible formulation allows for a much larger time step, not only because of the lack of acoustics but also because of the implicit temporal discretization of the viscous terms in the momentum equations. However, it is important to remember that a time step of our GPU-parallelized compressible code takes much less computing than a time step of the incompressible code. Nevertheless, we are able to study larger system sizes in three dimensions using the incompressible algorithm. In the incompressible simulations, we used (36) for the velocity equation in order to avoid unnecessary projections. Because of the explicit handling of the concentration boundary conditions, we employed a predictor-corrector algorithm for the concentration equation, in which both the predictor and the corrector stages have the form (37).

In Figure 7 we show numerical results for the steady-state spectrum of the discrete concentration field averaged along the y axes, in two dimensions (left panel) and in three dimensions (right panel), for both bulk (quasi-periodic) and finite (nonperiodic) systems. In order to compare with the theoretical predictions (58) and (59)

most directly, we plot the ratio of the observed to the predicted spectrum. This choice of normalization not only emphasizes any mismatch with the theory but also eliminates the power-law ($k_\perp^{-4}$) divergence and makes it easier to average over nearby wavenumbers $\tilde{k}_\perp$ and also estimate error bars.[1] For the runs reported in Figure 7 we applied the largest concentration (temperature) gradient ($\Delta T = 17.4$K) used in the experiments [12]; we have verified that the nonequilibrium concentration fluctuations scale as the square of the gradient.

Both panels in Figure 7 show an excellent agreement between the theory (58) and the numerical results for quasi-periodic systems. This shows that correcting for the spatial discretization artifacts by replacing $k_\perp$ with $\tilde{k}_\perp$ accounts for most of the discretization error. For the compressible runs, we use a relatively small time step, $\alpha = 0.2$, leading to temporal discretization errors that are smaller than the statistical accuracy except at the largest wavenumbers. Our semi-implicit discretization of the incompressible equations gives the correct static covariance of the concentration for *all* time step sizes. Based on the analysis presented in Appendix A, the majority of the incompressible simulations employ a time step corresponding to a viscous CFL number $\beta = 1$ or $\beta = 2$, with a few of the largest systems run at $\beta = 5$ to better resolve the smaller wavenumbers.

In the left panel of Figure 7 we compare results from two-dimensional compressible and incompressible simulations and find excellent agreement. For nonperiodic systems, the single-mode Galerkin theory (59) is not exact and the theory visibly overpredicts the concentration fluctuations for smaller wavenumbers in both two and three dimensions. We observe only a partial overlap of the data for different Schmidt numbers $S_c = \nu/\chi$ for smaller wavenumbers, although the difference between $S_c = 10$ and $S_c = 20$ is relatively small.

In three dimensions we rely on the incompressible code in order to reach time scales necessary to obtain sufficiently accurate steady-state averages for large Schmidt numbers. In the right panel of Figure 7 we compare numerical results for quasi-periodic and nonperiodic compressible and incompressible systems to the theoretical predictions and also to experimental data from [12, 86]. While the numerical data does not match the experiments precisely at the smallest wavenumbers, a more careful comparison is at present not possible. First, the boundary conditions affect the small wavenumbers strongly, and our use of periodic boundary conditions in the x and z directions does not match the experimental setup. The experimental data has substantial measurement uncertainties and is presently normalized by an arbitrary prefactor. Within this arbitrary normalization, our numerical results seem to be in good agreement with the experimental observations over the whole range of experimentally accessible wavenumbers, and the agreement at small wavenumbers improves as the Schmidt number of the simulations increases. The actual magnitude of the *macroscopic* nonequilibrium fluctuations in $c_\perp$ is given by the integral of the structure factor $S_{c,c}^{\perp}$ over all wavenumbers $\boldsymbol{k}_\perp$. Numerically we observe fluctuations $\left\langle (\delta c_\perp)^2 \right\rangle / \bar{c}_\perp^2 \approx 3 \cdot 10^{-7}$, which is consistent with experimental estimates [86].

6. Conclusions. We have presented spatio-temporal discretizations of the equations of fluctuating hydrodynamics for both compressible and incompressible mixtures of dynamically identical isothermal fluids. As proposed by some of us in [28], we judge the weak accuracy of the schemes by their ability to reproduce the equilibrium co-

[1] Note, however, that the most reliable error bars are obtained by averaging over many *uncorrelated* runs started with different random number seeds.

variances of the fluctuating variables. In particular, for small time steps the spatial discretization ensures that each mode is equally forced and dissipated in agreement with the fluctuation-dissipation balance principle satisfied by the continuum equations. A crucial ingredient of this discrete fluctuation-dissipation balance is the use of a discrete Laplacian $\boldsymbol{L} = -\boldsymbol{D}\boldsymbol{D}^\star$ for the dissipative fluxes, where $\boldsymbol{D}$ is a conservative discrete divergence, with a suitable correction to both the Laplacian stencil and the stochastic fluxes at physical boundaries. Furthermore, we utilize a centered skew-adjoint discretization of advection which does not additionally dissipate or force the fluctuations, as previously employed in long-time simulations of turbulent flow, where it is also crucial to ensure conservation and avoid artificial dissipation [77].

For the compressible equations, our spatio-temporal discretization is closely based on the collocated scheme proposed by some of us in [28], except that here we employ a staggered velocity grid. It is important to point out the difference between a *collocated* scheme, in which the fluid variables are cell-centered but the stochastic fluxes are face-centered (staggered), as described in [28], and a *centered* scheme where *all* quantities are cell-centered. Several authors [26, 27] have already noted that centered schemes lead to a Laplacian that decouples neighboring cells, which is problematic in the context of fluctuating hydrodynamics. We emphasize, however, that these problems are not shared by collocated schemes for compressible fluids, for which the Laplacian $\boldsymbol{L} = -\boldsymbol{D}\boldsymbol{D}^\star$ has the usual compact $2d+1$ stencil, where d is the dimensionality [28]. Discretizations in which all conserved quantities are collocated may be preferred over staggered ones in particle-continuum hybrids [13] or, more generally, in conservative discretizations for nonuniform grids.

A staggered grid arrangement, however, has a distinct advantage for incompressible flow. Namely, the use of a staggered grid simplifies the construction of a robust idempotent discrete projection $\mathbb{P} = \boldsymbol{I} + \boldsymbol{D}^\star \boldsymbol{L}^{-1} \boldsymbol{D}$ that maintains discrete fluctuation-dissipation at all wavenumbers. In the temporal discretization employed here, based on prior work by one of us [34], this projection is used as a preconditioner for solving the Stokes equations for the pressure and velocities at the next time step. For periodic systems, the method becomes equivalent to a classical Crank–Nicolson-based projection method, while at the same time avoiding the appearance of artificial pressure modes in the presence of physical boundaries [71, 72].

The numerical results presented in section 5 verify that our numerical simulations model experimental measurements of giant fluctuations [12] during diffusive mixing of fluids faithfully. The numerical simulations give access to a lot more data than is experimentally measurable. For example, the spectrum of concentration fluctuations in the x-z plane can be computed for planes (slices) as the distance from the boundaries is varied, giving a more complete picture of the three-dimensional spatial correlations of the nonequilibrium fluctuations. We defer a more detailed analysis, including a study of temporal correlations, to future work.

The compressible solver we developed utilizes modern GPUs for accelerating the computations. In the future we will investigate the use of GPUs for the incompressible equations for nonperiodic systems. For grid sizes that are much larger than molecular scales, the stability restriction of explicit compressible solvers becomes severe and it becomes necessary to eliminate sound waves from the equations by employing the low Mach number limit. A challenge that remains to be addressed in future work is the design of zero Mach number methods [48] for solving the variable-density equations of fluctuating hydrodynamics, as necessary when modeling mixtures of miscible fluids with different densities. This would enable computational modeling of the effects

of buoyancy (gravity) in experimental studies of the giant fluctuation phenomenon performed on Earth [39, 42, 43].

Appendix A. Implicit midpoint rule as a Gibbs sampler. We consider here numerical methods for the general additive-noise linear SDE

$$\frac{d\boldsymbol{x}}{dt} = \boldsymbol{A}\boldsymbol{x} + \boldsymbol{K}\boldsymbol{\mathcal{W}}(t), \tag{A1}$$

where $\boldsymbol{\mathcal{W}}(t)$ denotes white noise. If the eigenvalues of $\boldsymbol{A}$ have negative real parts, the long-time dynamics tends to a Gaussian equilibrium distribution

$$P_{\mathrm{eq}}(\boldsymbol{x}) = Z^{-1} \exp\left(-\frac{\boldsymbol{x}^\star \boldsymbol{S}^{-1}\boldsymbol{x}}{2}\right), \tag{A2}$$

where the covariance matrix $\boldsymbol{S}$ is the solution to the linear system (see, for example, equation (30) in [28] or equation (3.10) in [64])

$$\boldsymbol{A}\boldsymbol{S} + \boldsymbol{S}\boldsymbol{A}^\star = -\boldsymbol{K}\boldsymbol{K}^\star. \tag{A3}$$

If one is interested only in calculating steady-state observables (expectation values), then a numerical method for solving (A1) needs to sample only the equilibrium Gibbs distribution (A2), without having to approximate the correct dynamics.

The implicit midpoint rule or Crank–Nicolson discretization that we employed in section 3.1.2,

$$\boldsymbol{x}^{n+1} = \boldsymbol{x}^n + \boldsymbol{A}\left(\frac{\boldsymbol{x}^n + \boldsymbol{x}^{n+1}}{2}\right)\Delta t + \Delta t^{1/2}\boldsymbol{K}\boldsymbol{W}^n, \tag{A4}$$

can be seen as a Markov chain Monte Carlo (MCMC) algorithm for sampling from the distribution (A2). This sampling is exact; that is, the equilibrium distribution of the chain (A4) is exactly (A2). This important fact can be shown using the techniques described in [28], but here we present an alternative derivation.

A well-known MCMC algorithm for sampling the Gibbs distribution is the Metropolis–Hastings algorithm. In this algorithm, one treats $\boldsymbol{x}^{n+1}$ as a *trial* or *proposal* move that is then to be accepted with probability

$$\alpha = \frac{P_{\mathrm{eq}}\left(\boldsymbol{x}^{n+1}\right)}{P_{\mathrm{eq}}\left(\boldsymbol{x}^n\right)} \frac{P_{\mathrm{rev}}\left(\boldsymbol{x}^{n+1} \to \boldsymbol{x}^n\right)}{P_{\mathrm{forw}}\left(\boldsymbol{x}^n \to \boldsymbol{x}^{n+1}\right)},$$

where P_{forw} is the transition probability for the chain (A4) and P_{rev} is the transition probability for the *time-reversed* chain (this important distinction ensures strict time reversibility of the chain with respect to the equilibrium distribution). Explicitly,

$$P_{\mathrm{rev}}\left(\boldsymbol{x}^{n+1} \to \boldsymbol{x}^n\right) = C \exp\left[-\frac{\left(\boldsymbol{W}^n\right)^\star \left(\boldsymbol{W}^n\right)}{2}\right],$$

$$P_{\mathrm{forw}}\left(\boldsymbol{x}^n \to \boldsymbol{x}^{n+1}\right) = C \exp\left[-\frac{\left(\widetilde{\boldsymbol{W}}^n\right)^\star \left(\widetilde{\boldsymbol{W}}^n\right)}{2}\right],$$

where the reverse step noise $\widetilde{\boldsymbol{W}}^n$ is the solution to the equation (here the adjoint of $\boldsymbol{A}$ appears because of time reversal)

$$\boldsymbol{x}^n = \boldsymbol{x}^{n+1} + \boldsymbol{A}^\star\left(\frac{\boldsymbol{x}^n + \boldsymbol{x}^{n+1}}{2}\right)\Delta t + \Delta t^{1/2}\boldsymbol{K}\widetilde{\boldsymbol{W}}^n.$$

Note that the case of noninvertible $\boldsymbol{K}$ can be easily handled by working not with the random flux $\boldsymbol{W}^n$ but rather with the stochastic increments $\boldsymbol{K}\boldsymbol{W}^n$, whose covariance $\boldsymbol{K}\boldsymbol{K}^\star$ can be assumed to be invertible without loss of generality.

A tedious but straightforward matrix calculation shows that the acceptance probability $\alpha = 1$; that is, no rejection is necessary for the implicit midpoint rule to sample the correct equilibrium distribution, *regardless* of the time step Δt. The calculation of α is simple to do if a Fourier transform is used to diagonalize the hydrodynamic equations (see (19)) to obtain a system of scalar SDEs with complex coefficients. For the stochastic advection-diffusion equation (38) with $\boldsymbol{v} = v_0$, which is a good model for more general hydrodynamic equations,

$$\boldsymbol{A} \equiv A = -a + b\,i, \quad \boldsymbol{K} \equiv K = \sqrt{2a}, \quad \boldsymbol{S} \equiv S = 1, \tag{A5}$$

with $a = \chi k^2$ and $b = -kv_0$, where k is the wavenumber.

While the time step Δt can be chosen arbitrarily without biasing the sampling, the optimal choice is the one that minimizes the variance of the Monte Carlo estimate of the observable of interest. In the simulations of giant fluctuation experiments, the observable of interest is the covariance (spectrum) of the fluctuations $\boldsymbol{S} = \langle \boldsymbol{x}\boldsymbol{x}^\star \rangle$. The variance of the Monte Carlo estimate of $\boldsymbol{S}$ is proportional to the autocorrelation time τ of $\boldsymbol{S}^n = \boldsymbol{x}^n\,(\boldsymbol{x}^n)^\star$, which itself is proportional to the sum of the autocorrelation function of $\boldsymbol{S}^n$ [87]. Focusing on the scalar SODE (A5), we get the autocorrelation time

$$\tau \sim \sum_{n=0}^{\infty} \left[\left\langle S^k S^{k+n} \right\rangle - \left\langle S^k \right\rangle^2 \right] = \sum_{n=0}^{\infty} (AA^\star)^n = \frac{1}{2a\Delta t} + \frac{1}{2} + \frac{a\Delta t}{8} + \frac{b\Delta t}{a}.$$

For the purely diffusive equation, $v_0 = 0$, the statistical accuracy for a fixed number of time steps is proportional to

$$\tau^{-1} = \frac{8\tilde{k}^2\beta}{4 + 4\tilde{k}^2\beta + \tilde{k}^4\beta^2},$$

where $\beta = \nu\Delta t/\Delta x^2$ is the viscous CFL number and $\tilde{k} = k\Delta x$ is the dimensionless wavenumber. Note that $\tau^{-1} \sim \beta\tilde{k}^2$ for small $\tilde{k}$, so increasing the time step improves the sampling. However, for large $\tilde{k}$, increasing the time step reduces the statistical accuracy (this is related to the fact that the Crank–Nicolson algorithm is A-stable but *not* L-stable), $\tau^{-1} \sim \left(\beta\tilde{k}^2\right)^{-1}$. The wavenumber with the highest statistical accuracy $\tilde{k}_{\text{opt}}$ depends on the time step, $\beta\tilde{k}_{\text{opt}}^2 = 2$, or, alternatively, the optimal choice of time step depends on the wavenumber of most interest. For the type of problems we studied in this work, the spectrum of the fluctuations has power-law tails $\sim k^{-4}$, and therefore all wavenumbers are important. Using $\beta \sim 2$ produces a good coverage of all of the wavenumbers.

Appendix B. Fluctuation-dissipation balance for incompressible flow. Discrete fluctuation-dissipation balance is affected by the presence of an incompressibility constraint. The spatially discretized velocity equation linearized around a stationary equilibrium state has the form, omitting unimportant constants in the noise amplitude,

$$\partial_t \boldsymbol{v} = \mathbb{P}\left[\nu \boldsymbol{L}\boldsymbol{v} + \sqrt{2\nu}\boldsymbol{D}\boldsymbol{W}_{\boldsymbol{v}}\right], \tag{B1}$$

where we used a nonsymmetric stochastic stress tensor since the symmetry does not affect the results presented here. The steady-state covariance of the velocities $\boldsymbol{S_v} = \langle \boldsymbol{v}\boldsymbol{v}^\star \rangle$ is determined from the fluctuation-dissipation balance condition (A3) with $\boldsymbol{A} = \nu \mathbb{P}\boldsymbol{L}$ and $\boldsymbol{K} = \sqrt{2\nu}\,\mathbb{P}\boldsymbol{D}$, giving

$$\mathbb{P}\boldsymbol{L}\boldsymbol{S_v} + \boldsymbol{S_v}\boldsymbol{L}^\star\mathbb{P}^\star = -2\mathbb{P}\boldsymbol{D}\boldsymbol{D}^\star\mathbb{P}^\star. \tag{B2}$$

The fluctuation-dissipation balance condition for the simple advection-diffusion equation

$$\boldsymbol{L} + \boldsymbol{L}^\star = \boldsymbol{D}\boldsymbol{G} + (\boldsymbol{D}\boldsymbol{G})^\star = -2\boldsymbol{D}\boldsymbol{D}^\star$$

implies that $\boldsymbol{S_v} = \mathbb{P}$ is the solution to (B2) if $\mathbb{P}$ is self-adjoint, $\mathbb{P}^\star = \mathbb{P}$, as stated in (45) with all of the constants included.

The above analysis does not account for the temporal discretization. For small time steps, our temporal discretization of (B1) behaves similarly to a projected Euler–Maruyama method:

$$\boldsymbol{v}^{n+1} = \mathbb{P}\left[\boldsymbol{v}^n + \nu\boldsymbol{L}\boldsymbol{v}\Delta t + \sqrt{2\nu\Delta t}\boldsymbol{D}\boldsymbol{W}_{\boldsymbol{v}}\right].$$

An important difference with the continuum equation (B1) is that the velocity in the previous time step is also projected; i.e., the increment of $O(\Delta t)$ is added to $\mathbb{P}\boldsymbol{v}^n$ and *not* to $\boldsymbol{v}^n$. If $\mathbb{P}$ is idempotent, $\mathbb{P}^2 = \mathbb{P}$, just as the continuum projection operator is, then subsequent applications of the projection operator do not matter since $\boldsymbol{v}^n$ is already discretely divergence-free, $\mathbb{P}\boldsymbol{v}^n = \boldsymbol{v}^n$. In the literature on projection methods idempotent projections are called *exact* projections.

The above considerations lead to the conclusion that $\boldsymbol{S_v} = \mathbb{P}$ if $\mathbb{P}^\star = \mathbb{P}$ and $\mathbb{P}^2 = \mathbb{P}$. Both of these conditions are met by the MAC discrete projection operator $\mathbb{P} = \boldsymbol{I} - \boldsymbol{D}^\star(\boldsymbol{D}\boldsymbol{D}^\star)^{-1}\boldsymbol{D}$, which shows that our spatio-temporal discretization gives velocity fluctuations that have the correct covariance (45). A straightforward extension of the analysis in Appendix A shows that the Crank–Nicolson temporal discretization (36) gives the correct equilibrium velocity covariance for *any* time step size, not just for small time steps. Further details will be presented in future publications [46].

Acknowledgments. We thank Alberto Vailati for insightful comments and sharing experimental data from the GRADFLEX experiments [12]. We thank Alejandro Garcia for a careful reading and suggestions on improving this work. We thank Eric Vanden-Eijnden and Jonathan Goodman for numerous inspiring discussions and motivating the Metropolis–Hastings Monte Carlo argument presented in Appendix A. A. Donev thanks the NVIDIA Academic Partnership program for providing GPU hardware for performing some of the simulations reported here.

REFERENCES

[1] L. Bocquet and E. Charlaix, *Nanofluidics, from bulk to interfaces*, Chem. Soc. Rev., 39 (2010), pp. 1073–1095.

[2] L. Wang and M. Quintard, *Nanofluids of the future*, in Advances in Transport Phenomena, Springer-Verlag, Berlin, Heidelberg, 2009, pp. 179–243.

[3] A. Naji, P. J. Atzberger, and F. L. H. Brown, *Hybrid elastic and discrete-particle approach to biomembrane dynamics with application to the mobility of curved integral membrane proteins*, Phys. Rev. Lett., 102 (2009), 138102.

[4] C. S. Peskin, G. M. Odell, and G. F. Oster, *Cellular motions and thermal fluctuations: The Brownian ratchet*, Biophys. J., 65 (1993), pp. 316–324.

[5] F. Detcheverry and L. Bocquet, *Thermal fluctuations in nanofluidic transport*, Phys. Rev. Lett., 109 (2012), 024501.
[6] R. Delgado-Buscalioni, E. Chacon, and P. Tarazona, *Hydrodynamics of nanoscopic capillary waves*, Phys. Rev. Lett., 101 (2008), 106102.
[7] B. Z. Shang, N. K. Voulgarakis, and J.-W. Chu, *Fluctuating hydrodynamics for multiscale simulation of inhomogeneous fluids: Mapping all-atom molecular dynamics to capillary waves*, J. Chem. Phys., 135 (2011), 044111.
[8] M. Moseler and U. Landman, *Formation, stability, and breakup of nanojets*, Science, 289 (2000), pp. 1165–1169.
[9] B. Davidovitch, E. Moro, and H. A. Stone, *Spreading of viscous fluid drops on a solid substrate assisted by thermal fluctuations*, Phys. Rev. Lett., 95 (2005), 244505.
[10] Y. Hennequin, D. G. A. L. Aarts, J. H. van der Wiel, G. Wegdam, J. Eggers, H. N. W. Lekkerkerker, and D. Bonn, *Drop formation by thermal fluctuations at an ultralow surface tension*, Phys. Rev. Lett., 97 (2006), 244502.
[11] A. Donev, A. L. Garcia, A. de la Fuente, and J. B. Bell, *Diffusive transport by thermal velocity fluctuations*, Phys. Rev. Lett., 106 (2011), 204501.
[12] A. Vailati, R. Cerbino, S. Mazzoni, C. J. Takacs, D. S. Cannell, and M. Giglio, *Fractal fronts of diffusion in microgravity*, Nat. Comm., 2 (2011), 290.
[13] A. Donev, J. B. Bell, A. L. Garcia, and B. J. Alder, *A hybrid particle-continuum method for hydrodynamics of complex fluids*, Multiscale Model. Simul., 8 (2010), pp. 871–911.
[14] C. W. Gardiner, *Handbook of Stochastic Methods: For Physics, Chemistry and the Natural Sciences*, 3rd ed., Springer Ser. Synergetics 13, Springer-Verlag, Berlin, 2004.
[15] N. G. van Kampen, *Stochastic Processes in Physics and Chemistry*, 3rd ed., Elsevier, Amsterdam, 2007.
[16] L. D. Landau and E. M. Lifshitz, *Fluid Mechanics*, Course of Theoretical Physics 6, Pergamon Press, Oxford, England, 1959.
[17] J. M. O. De Zarate and J. V. Sengers, *Hydrodynamic Fluctuations in Fluids and Fluid Mixtures*, Elsevier Science, New York, 2006.
[18] A. L. Garcia, M. M. Mansour, G. Lie, and E. Clementi, *Numerical integration of the fluctuating hydrodynamic equations*, J. Stat. Phys., 47 (1987), pp. 209–228.
[19] B. Dunweg and A. J. C. Ladd, *Lattice Boltzmann simulations of soft matter systems*, in Advanced Computer Simulation Approaches for Soft Matter Sciences III, Springer-Verlag, Berlin, Heidelberg, 2009, pp. 89–166.
[20] N. Sharma and N. A. Patankar, *Direct numerical simulation of the Brownian motion of particles by using fluctuating hydrodynamic equations*, J. Comput. Phys., 201 (2004), pp. 466–486.
[21] G. De Fabritiis, M. Serrano, R. Delgado-Buscalioni, and P. V. Coveney, *Fluctuating hydrodynamic modeling of fluids at the nanoscale*, Phys. Rev. E, 75 (2007), 026307.
[22] G. Giupponi, G. De Fabritiis, and P. V. Coveney, *Hybrid method coupling fluctuating hydrodynamics and molecular dynamics for the simulation of macromolecules*, J. Chem. Phys., 126 (2007), 154903.
[23] R. Delgado-Buscalioni and G. De Fabritiis, *Embedding molecular dynamics within fluctuating hydrodynamics in multiscale simulations of liquids*, Phys. Rev. E, 76 (2007), 036709.
[24] P. J. Atzberger, P. R. Kramer, and C. S. Peskin, *A stochastic immersed boundary method for fluid-structure dynamics at microscopic length scales*, J. Comput. Phys., 224 (2007), pp. 1255–1292.
[25] P. J. Atzberger, *Stochastic Eulerian-Lagrangian methods for fluid-structure interactions with thermal fluctuations*, J. Comput. Phys., 230 (2011), pp. 2821–2837.
[26] N. K. Voulgarakis and J.-W. Chu, *Bridging fluctuating hydrodynamics and molecular dynamics simulations of fluids*, J. Chem. Phys., 130 (2009), 134111.
[27] R. Delgado-Buscalioni and A. Dejoan, *Nonreflecting boundaries for ultrasound in fluctuating hydrodynamics of open systems*, Phys. Rev. E, 78 (2008), 046708.
[28] A. Donev, E. Vanden-Eijnden, A. L. Garcia, and J. B. Bell, *On the accuracy of explicit finite-volume schemes for fluctuating hydrodynamics*, Commun. Appl. Math. Comput. Sci., 5 (2010), pp. 149–197.
[29] J. B. Bell, A. L. Garcia, and S. A. Williams, *Numerical methods for the stochastic Landau-Lifshitz Navier-Stokes equations*, Phys. Rev. E, 76 (2007), 016708.
[30] J. B. Bell, A. Garcia, and S. Williams, *Computational fluctuating fluid dynamics*, M2AN Math. Model. Numer. Anal., 44 (2010), pp. 1085–1105.
[31] A. Donev, A. L. Garcia, A. de la Fuente, and J. B. Bell, *Enhancement of diffusive transport by nonequilibrium thermal fluctuations*, J. Stat. Mech. Theory Exp., 2011 (2011), P06014.

[32] S. V. Patankar, *Numerical Heat Transfer and Fluid Flow*, Hemisphere, New York, 1980.
[33] B. E. Griffith, *On the volume conservation of the immersed boundary method*, Commun. Comput. Phys., 12 (2012), pp. 401–432.
[34] B. E. Griffith, *An accurate and efficient method for the incompressible Navier-Stokes equations using the projection method as a preconditioner*, J. Comput. Phys., 228 (2009), pp. 7565–7595.
[35] A. L. Garcia, M. M. Mansour, G. C. Lie, M. Mareschal, and E. Clementi, *Hydrodynamic fluctuations in a dilute gas under shear*, Phys. Rev. A, 36 (1987), pp. 4348–4355.
[36] M. Mareschal, M. M. Mansour, G. Sonnino, and E. Kestemont, *Dynamic structure factor in a nonequilibrium fluid: A molecular-dynamics approach*, Phys. Rev. A, 45 (1992), pp. 7180–7183.
[37] J. R. Dorfman, T. R. Kirkpatrick, and J. V. Sengers, *Generic long-range correlations in molecular fluids*, Annu. Rev. Phys. Chem., 45 (1994), pp. 213–239.
[38] J. M. Ortiz de Zarate and J. V. Sengers, *On the physical origin of long-ranged fluctuations in fluids in thermal nonequilibrium states*, J. Stat. Phys., 115 (2004), pp. 1341–1359.
[39] A. Vailati and M. Giglio, *Nonequilibrium fluctuations in time-dependent diffusion processes*, Phys. Rev. E, 58 (1998), pp. 4361–4371.
[40] C. J. Takacs, G. Nikolaenko, and D. S. Cannell, *Dynamics of long-wavelength fluctuations in a fluid layer heated from above*, Phys. Rev. Lett., 100 (2008), 234502.
[41] D. Brogioli, *Giant Fluctuations in Diffusion in Freely-Suspended Liquid Films*, ArXiv e-prints, 2011.
[42] A. Vailati and M. Giglio, *Giant fluctuations in a free diffusion process*, Nature, 390 (1997), pp. 262–265.
[43] D. Brogioli, A. Vailati, and M. Giglio, *Universal behavior of nonequilibrium fluctuations in free diffusion processes*, Phys. Rev. E, 61 (2000), pp. 1–4.
[44] A. Vailati, R. Cerbino, S. Mazzoni, M. Giglio, G. Nikolaenko, C. J. Takacs, D. S. Cannell, W. V. Meyer, and A. E. Smart, *Gradient-driven fluctuations experiment: Fluid fluctuations in microgravity*, Appl. Optic., 45 (2006), pp. 2155–2165.
[45] F. Croccolo, D. Brogioli, A. Vailati, M. Giglio, and D. S. Cannell, *Nondiffusive decay of gradient-driven fluctuations in a free-diffusion process*, Phys. Rev. E, 76 (2007), 041112.
[46] S. Delong, B. E. Griffith, E. Vanden-Eijnden, and A. Donev, *Temporal Integrators for Fluctuating Hydrodynamics*, manuscript, 2012.
[47] F. Balboa Usabiaga, I. Pagonabarraga, and R. Delgado-Buscalioni, *Inertial Coupling for Point Particle Fluctuating Hydrodynamics*, manuscript, 2011.
[48] T. Alazard, *A minicourse on the low Mach number limit*, Discrete Contin. Dyn. Syst. Ser. S, 1 (2008), pp. 365–404.
[49] B. Muller, *Low-Mach-number asymptotics of the Navier-Stokes equations*, J. Engrg. Math., 34 (1998), pp. 97–109.
[50] J. Lowengrub and L. Truskinovsky, *Quasi-incompressible Cahn-Hilliard fluids and topological transitions*, R. Soc. Lond. Proc. Ser. A Math. Phys. Eng. Sci., 454 (1998), pp. 2617–2654.
[51] P. Español, *Stochastic differential equations for non-linear hydrodynamics*, Phys. A, 248 (1998), pp. 77–96.
[52] J. L. Lebowitz, E. Orlanndi, and E. Presutti, *Convergence of stochastic cellular automation to Burgers' equation: Fluctuations and stability*, Phys. D, 33 (1988), pp. 165–188.
[53] L. Bertini and G. Giacomin, *Stochastic Burgers and KPZ equations from particle systems*, Comm. Math. Phys., 183 (1997), pp. 571–607.
[54] R. Kubo, *The fluctuation-dissipation theorem*, Rep. Progr. Phys., 29 (1966), pp. 255–284.
[55] H. C. Öttinger, H. Struchtrup, and M. Liu, *Inconsistency of a dissipative contribution to the mass flux in hydrodynamics*, Phys. Rev. E, 80 (2009), 056303.
[56] H. C. Ottinger, *Beyond Equilibrium Thermodynamics*, Wiley Online Library, 2005.
[57] P. Español, J. G. Anero, and I. Zúñiga, *Microscopic derivation of discrete hydrodynamics*, J. Chem. Phys., 131 (2009), 244117.
[58] D. Bedeaux and P. Mazur, *Renormalization of the diffusion coefficient in a fluctuating fluid* I, Physica, 73 (1974), pp. 431–458.
[59] G. Da Prato, *Kolmogorov Equations for Stochastic PDEs*, Birkhäuser, Basel, 2004.
[60] N. K. Ailawadi, B. J. Berne, and D. Forster, *Hydrodynamics and collective angular-momentum fluctuations in molecular fluids*, Phys. Rev. A, 3 (1971), pp. 1462–1472.
[61] J. S. Hansen, J. C. Dyre, P. J. Daivis, B. D. Todd, and H. Bruus, *Nanoflow hydrodynamics*, Phys. Rev. E, 84 (2011), 036311.
[62] J. M. Ortiz de Zárate, F. Peluso, and J. V. Sengers, *Nonequilibrium fluctuations in the Rayleigh-Bénard problem for binary fluid mixtures*, Eur. Phys. J. E, 15 (2004), pp. 319–333.

[63] L. D. Landau and E. M. Lifshitz, *Statistical Physics*, Course of Theoretical Physics 5, 3rd ed., Part 1, Pergamon Press, Oxford, England, 1980.
[64] P. J. Atzberger, *Spatially adaptive stochastic numerical methods for intrinsic fluctuations in reaction-diffusion systems*, J. Comput. Phys., 229 (2010), pp. 3474–3501.
[65] D. Brogioli and A. Vailati, *Diffusive mass transfer by nonequilibrium fluctuations: Fick's law revisited*, Phys. Rev. E, 63 (2000), 12105.
[66] S. Gottlieb, C.-W. Shu, and E. Tadmor, *Strong stability-preserving high-order time discretization methods*, SIAM Rev., 43 (2001), pp. 89–112.
[67] S. Gottlieb and C. Shu, *Total variation diminishing Runge-Kutta schemes*, Math. Comp., 67 (1998), pp. 73–85.
[68] K. Debrabant, *Runge-Kutta methods for third order weak approximation of SDEs with multidimensional additive noise*, BIT, 50 (2010), pp. 541–558.
[69] J. B. Bell, P. Colella, and H. M. Glaz, *A second order projection method for the incompressible Navier-Stokes equations*, J. Comput. Phys., 85 (1989), pp. 257–283.
[70] A. S. Almgren, J. B. Bell, and W. G. Szymczak, *A numerical method for the incompressible Navier–Stokes equations based on an approximate projection*, SIAM J. Sci. Comput., 17 (1996), pp. 358–369.
[71] W. E and J. G. Liu, *Projection method* III: *Spatial discretization on the staggered grid*, Math. Comp., 71 (2002), pp. 27–48.
[72] W. E and J. G. Liu, *Gauge method for viscous incompressible flows*, Commun. Math. Sci., 1 (2003), pp. 317–332.
[73] T. Li, A. Abdulle, and W. E, *Effectiveness of implicit methods for stiff stochastic differential equations*, Commun. Comput. Phys., 3 (2008), pp. 295–307.
[74] J. C. Mattingly, A. M. Stuart, and M. V. Tretyakov, *Convergence of numerical time-averaging and stationary measures via Poisson equations*, SIAM J. Numer. Anal., 48 (2010), pp. 552–557.
[75] A. S. Almgren, J. B. Bell, and W. Y. Crutchfield, *Approximate projection methods: Part* I. *Inviscid analysis*, SIAM J. Sci. Comput., 22 (2000), pp. 1139–1159.
[76] F. H. Harlow and J. E. Welch, *Numerical calculation of time-dependent viscous incompressible flow of fluids with free surfaces*, Phys. Fluids, 8 (1965), pp. 2182–2189.
[77] Y. Morinishi, T. S. Lund, O. V. Vasilyev, and P. Moin, *Fully conservative higher order finite difference schemes for incompressible flow*, J. Comput. Phys., 143 (1998), pp. 90–124.
[78] Y. Morinishi, *Skew-symmetric form of convective terms and fully conservative finite difference schemes for variable density low-Mach number flows*, J. Comput. Phys., 229 (2010), pp. 276–300.
[79] J. D. Ramshaw and K. Lindenberg, *Augmented Langevin description of multiplicative noise and nonlinear dissipation in Hamiltonian systems*, J. Statist. Phys., 45 (1986), pp. 295–307.
[80] B. E. Griffith, R. D. Hornung, D. M. McQueen, and C. S. Peskin, *An adaptive, formally second order accurate version of the immersed boundary method*, J. Comput. Phys., 223 (2007), pp. 10–49; software available online from http://ibamr.googlecode.com.
[81] R. D. Hornung, A. M. Wissink, and S. R. Kohn, *Managing complex data and geometry in parallel structured AMR applications*, Eng. Comput., 22 (2006), pp. 181–195; software available online from https://computation.llnl.gov/casc/SAMRAI.
[82] S. Balay, W. D. Gropp, L. C. McInnes, and B. F. Smith, *Efficient management of parallelism in object oriented numerical software libraries*, in Modern Software Tools in Scientific Computing, E. Arge, A. M. Bruaset, and H. P. Langtangen, eds., Birkhäuser, Basel, 1997, pp. 163–202; software available online from http://www.mcs.anl.gov/petsc.
[83] R. Falgout, J. Jones, and U. Yang, *The design and implementation of hypre, a library of parallel high performance preconditioners*, in Numerical Solution of Partial Differential Equations on Parallel Computers, Springer-Verlag, Berlin, 2006, pp. 267–294; software available online from http://www.llnl.gov/CASC/hypre.
[84] E. Vanden-Eijnden, *private communication*, 2011.
[85] W. E, W. Ren, and E. Vanden-Eijnden, *A general strategy for designing seamless multiscale methods*, J. Comput. Phys., 228 (2009), pp. 5437–5453.
[86] A. Vailati, *private communication*, 2011.
[87] A. D. Sokal, *Monte Carlo methods in statistical mechanics: Foundations and new algorithms*, in Functional Integration, Plenum, New York, 1997, pp. 131–192.